Superfluid helium-3 in cylindrical restricted geometries : a study with low-frequency NMR

Benningshof, O.W.B.

Chapter 4

Helium-3 in nanosized cylinders

4.1 Introduction

The spatial size of the Cooper pairs corresponds to its coherence lengths as given by equation (1.33) and (1.34). Sizes could be regulated by changing the pressure and/or the temperature of the liquid. Values of the coherence lengths for different pressures at zero temperature are given in table 4.1 [84]. If the dimensions of the experimental container are large compared to these lengths the superfluid phases are expected to be the same as in the bulk system. However, if one reduces the size of the container to a few times the coherence length, one can suppress the superfluid behavior. By reducing only one dimension of the container (to the size of a few coherence lengths), hence a slab geometry, one can make a quasi-2D system. This geometry is theoretically considered by several authors, for example [85], [86], [87] and [88], who predicted that the A- or planar-phase [89] is the most stable phase [1] for low pressures at zero temperature. Recent experiments [90] and [91] indeed showed that the found phase in such geometry was A-phase like.

If we consider a geometry with two dimensions reduced, for example a long cylinder with a radius a few times the coherence length, one can expect a quasi-1D system. In such a system the superfluidity is suppressed in two directions. So, the superfluid property is only expected to be in one single direction (in both spin and orbital space), for which the polar state is expected. This state will be described in detail in the next section. The aim of our research is to experimentally investigate if this polar state exists in such cylinders, see section 4.5.2.

[1] Slab thickness should be around 300 - 700 nm.

P (bar)	ξ_0^* (nm)
0	50.1
3	32.8
6	25.1
9	20.7
12	18.0
15	16.0
18	14.4
21	13.3
24	12.3
27	11.5
30	10.9

Table 4.1: Typical values of $\xi_0^*(P)$. $\xi_0^* = \sqrt{3/5}\,\xi_0$.

4.2 Polar state

The unique feature of the polar state (for the first time described in [72]) is, compared to the other inert states that it is without broken relative symmetry; meaning that **S** and **L** do not need to be fixed in any relative configuration to minimize the energy. However, as they both have a preferred direction, the broken symmetry of the system is $S^2_{\mathbf{L}} \times S^2_{\mathbf{S}} \times U(1)_\phi$. The remaining symmetry is then $U(1)_{S_z} \times U(1)_{L_z}$, for which the order parameter (see section 1.4) is given by

$$A_{\mu j} = e^{i\phi} \begin{bmatrix} 0 & 0 & 0 \\ 0 & 0 & 0 \\ 0 & 0 & 1 \end{bmatrix}. \tag{4.1}$$

The anisotropic energy gap of this state, see figure 4.1, is given by

$$\mid \Delta_{\mathbf{k}} \mid = \Delta_0 \mid \cos\theta_{\mathbf{k}} \mid = \Delta_0 \mid \hat{\mathbf{w}} \cdot \hat{\mathbf{k}} \mid, \tag{4.2}$$

where $\hat{\mathbf{w}}$ is the conventional notation [2] of the preferred direction in orbital space of the polar state and Δ_0 the maximal value of the energy gap. At zero temperature the maximal value of the gap is $\Delta_0(0) \approx 2.02 k_B T_c$. The average value of the gap is obtained by multiplying Δ_0 with a factor [3] of $\sqrt{2/3}$. The temperature dependence of this anisotropic energy gap is expected to be similar to the case of the A-phase. The maximal value of the energy gap in the case of the A-phase [92] has the same temperature dependence as the B-phase, which is described in section A.2.

[2] For the Polar state it is conventional to notate the preferred direction of the order parameter in orbital space as $\hat{\mathbf{w}}$, which is notated as $\hat{\mathbf{l}}$ in the A-phase.

[3] The square root of the average of $\cos^2\theta$.

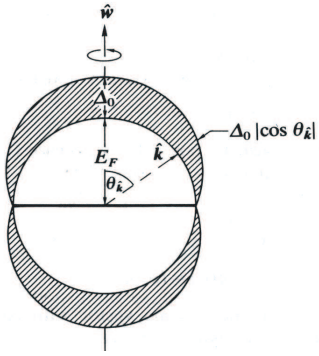

Figure 4.1: Scheme of the energy gap of the polar-phase in k-space indicated by the shaded area. The gap has rotation symmetry around $\hat{\mathbf{w}}$ and vanishes along the equator line. Ratio of Fermi energy E_F and the gap Δ_0 is not to scale. Figure is taken from [19].

4.2.1 Polar state in cylinders

Long narrow tubes would be an ideal candidate to expect a polar state. If the radius is limited to a few times the coherence length, two components of the order parameter are reduced enough that the polar state is energetically the expected phase. As in the polar state the energy is not determined by any relative position between the spin and orbital components, the preferred directions are determined by the geometry of the container and external magnetic field. In the case we deal with an external magnetic field parallel to the cylinder axis, we expect that the spins **S** will align along the axis of the cylinder (magnetic field) and the orbital component **L** perpendicular to the surface of the cylinder.

The (relatively) simple geometry makes it possible to predict in which conditions we would expect the polar state [86] [87] [93]. Barton and Moore calculated, for pores and cylinders with a radius R of the same order of magnitude as the coherence length, which phases could be expected. Two extreme conditions were considered: with complete diffuse scattering and with fully specular scattering boundary conditions. Cooling from the normal Fermi liquid phase, the following sequences are expected:

Diffuse scattering:
normal $\underrightarrow{2nd}$ polar $\underrightarrow{2nd}$ mixed axial $\underrightarrow{1st}$ transverse axial $\underrightarrow{1st}$ B-phase.

Specular scattering:
normal $\underrightarrow{2nd}$ polar $\underrightarrow{2nd}$ axial $\underrightarrow{1st}$ B-phase.

The order of each phase transition is indicated above the arrows. The variation of different phases is due to the competition of the terms in the free energy, which

Transition	α
normal $\rightarrow$ polar	2.40
polar $\rightarrow$ mixed axial	3.36
mixed axial $\rightarrow$ transverse axial (highest estimation)	3.83
mixed axial $\rightarrow$ transverse axial (lowest estimation)	6.04

Table 4.2: Estimation values of α for different transitions.

consist of bulk, surface and strain energy terms. For glass cylinders one would expect to be in the diffuse scattering regime, for which the authors have calculated the transition temperature as a function of the radius of the pores. The general expression they found is given by

$$T = T_c \left(1 - \frac{3}{5}\left(\frac{\xi_0}{R}\right)^2 \alpha^2\right), \tag{4.3}$$

where α is a dimensionless parameter depending on the phase, as listed in table 4.2. The mathematical complexity and increasing uncertainty of certain parameters at lower temperatures made it impossible for the authors to estimate one α corresponding to the mixed axial $\rightarrow$ transverse axial transition, and they were unable to determine it for the transition between the transverse axial $\rightarrow$ B-phase. However, as the coherence length is decreasing with further cooling, one expects to end in the (distorted) B-phase. By combining equation (4.3) and table 4.2 we can plot the expected transition temperatures as function of the ratio R/ξ_0, see graph 4.2.

All these calculations were performed in zero magnetic fields. A sufficiently large magnetic field would change the phase diagram and their sequences. Than the first expected phase will not be the polar-phase, but the so called β-phase [4]. As we are interested to find the polar phase, we apply a relatively low field (as in the case of the experiments described in chapter 3) to probe the superfluid with our NMR techniques.

An alternative calculation for the phase diagram for small cylindrical channels comes from Li and Ho [86]. Their calculations are based on the studies of Fishmann and Privorotskii [94] and Muzikar [95]. They found that in the case of sufficiently small channels the state with a polar core is most favorable. Their phase diagrams are calculated for long cylindrical channels with a radius R of 300 nm. Here they considered axial symmetric states, as it is believed that one of those should be the most favorable state.

Two 'confined conditions' are considered: $R \gg \xi(T)$ and $R \approx \xi(T)$, which are referred as 'mildly' and 'strongly' confined limits, respectively. As one goes from the strong to the mild regime, a transition from A polar state to B-like state should occur. They also included in their calculations the two scattering regimes (boundary conditions), specular (ideal mirror) and diffuse reflection, for which they constructed the accompanying phase diagrams.

[4] In this phase only up-up pairs are non-zero.

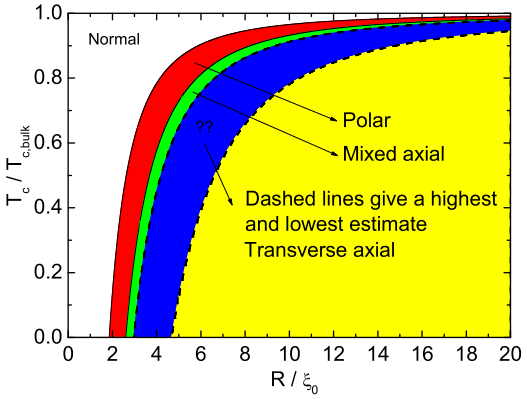

Figure 4.2: The reduced transition temperature of the expected phases in pores/cylinders as function of reduced radius. The red area indicates where the polar state is expected to be stable. The green area indicates the region where the mixed axial state is calculated to be the most favorable phase. Somewhere in the blue area the transition between mixed axial and transverse axial should occur. The transition temperature to the B-phase is unclear, but should happen at the lowest temperatures in the yellow area.

The boundary conditions are described in detail by Ambegaokar, deGennes and Rainer [89], who regard the spatial variations in the order parameter. Ambegaokar *et al.* consider the dominating term (quadratic term) of the gradient free energy density which is split into the longitudinal and transverse components (here the surface energy terms are neglected).

$$F_{grad} = \sum_p \{\frac{1}{2} K_L \mid \nabla \cdot \mathbf{A}_p \mid^2 + \frac{1}{2} K_T \mid \nabla \times \mathbf{A}_p \mid^2\}, \tag{4.4}$$

where the vector $\mathbf{A}_p$ has components A_{pi}. K_L and K_T are two positive coefficients and are related to the coherence length:

$$K_T = \frac{3}{5}\xi_0^2, \quad K_L - K_T = \frac{6}{5}\xi_0^2. \tag{4.5}$$

From which we define the longitudinal coherence length ξ_L and transverse coherence length ξ_T:

$$\xi_L^2 = 3\xi_T^2 = \frac{9}{5}\xi_0^2 \frac{T_c}{T_c - T}. \tag{4.6}$$

These authors solved the specular scattering problem for a (xy)-plane, with the ^{3}He only at one side ($z > 0$). The transverse components are parallel and the longitudinal component perpendicular to the plane.

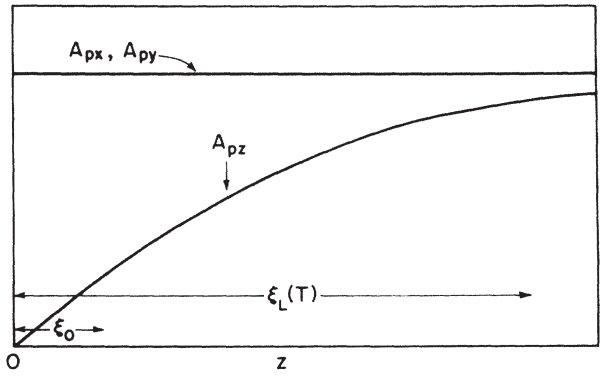

Figure 4.3: The transverse (A_{px}, A_{py}) and longitudinal (A_{pz}) components of the order parameter near a specular reflecting wall. Figure is taken from [89].

The most general solution at T_c is then:

$$A_{pi} = const \cdot (b_i + z) \quad (z \gg \xi_0), \tag{4.7}$$

which is asymptotically linear in z. For z near zero a more detailed calculation is needed to find the correct value of the extrapolation length b_i. If one considers the specular reflection at the wall, the solutions become:

$$A_{px} = A_{py} = const; \quad A_{pz} = const \cdot z. \tag{4.8}$$

The transverse components stay constant in the container, while the longitudinal component disappears at the wall. Both characteristics are plotted in figure 4.3.

In the case of diffuse reflection, the (transverse) components are reduced by a factor of $\xi_0/\xi(T)$. Here the longitudinal component still vanishes at the wall. Different is that the transverse order parameter components, at (and near) the transition temperature (of bulk), are zero at the wall (giving the reduction of the bulk T_c). However, for lower temperatures the transverse components get a finite amplitude (at the walls) again.

While the behavior of the components of the order parameter are derived in a semi-infinite volume, for which one component (longitudinal) vanishes at the wall, the analogy for a long cylinder is equivalent, and as one can imagine, not one but two components will vanish at the wall.

The reduction of the components of the order parameter, for geometries with the dimension of the order of the coherence length (e.g. slab geometries or small cylindrical channels), makes the B-phase unstable. If all the components, except one, are reduced, one intuitively can understand that the order parameter of the B-phase (1.15) should change to the polar phase (4.1).

The calculated (by Li and Ho) phase diagrams for long cylinders of radius R of 300 nm are plotted in the figures 4.4(a) and 4.4(b), for both boundary conditions:

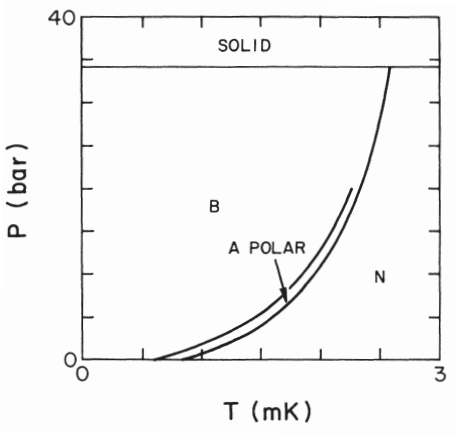

(a) The phase diagram of ^{3}He in a cylinder of radius $R = 300$ nm for diffusive boundary condition.

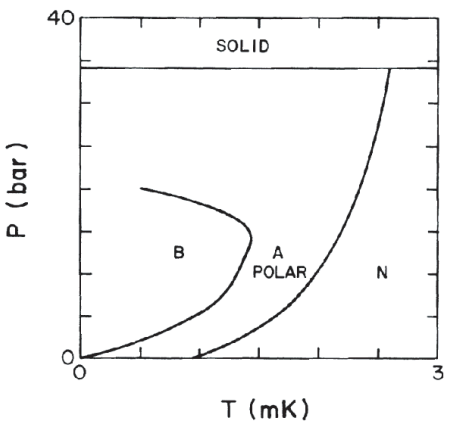

(b) The phase diagram of ^{3}He in a cylinder of radius $R = 300$ nm for specular boundary condition.

Figure 4.4: Figures taken from [86].

diffuse and specular, respectively. In contrast to slab geometries [86] the phase diagrams for the different boundary conditions are very different in the one-dimensional cylindrical geometry (the A-polar state exists in much wider region). In both cases the polar component is the most dominant part of the order parameter, which is mainly constant for specular scattering, but strongly suppressed for diffuse scattering. Also the temperatures at the phase boundary, separation between the normal and A-polar phase, is suppressed compared to the bulk situation for diffuse scattering. This suppression is given by:

$$T(P) = T_c(P)[1 - (\xi_0(P)/R)^2(1 + \pi^2/4)/(1 - 4/\pi^2)], \tag{4.9}$$

where T_c is the critical temperature of the bulk phase diagram. For specular boundary conditions the critical temperature is not reduced ($T(P) = T_c(P)$).

4.3 Photonic crystal fibers

To be able to measure a possible polar state one needs a cylinder with a diameter of roughly ten times the coherence length of the superfluid. In general it is not trivial to fabricate long cylinders with diameters of few hundred nanometers. To approach the semi one-dimensional geometry for superfluid helium-3, porous media have been used, see for example [96] and [97]. While it was possible to make pores with an average diameter of a few times the coherence length, the variance between them was rather high. Another problem is that the thickness of those samples was rather small (smaller than 1 mm). This made it impossible to perform a measurement which gives a direct and clean signal from the pores. Nevertheless, NMR, heat conducting, oscillation and sound experiments were performed on those samples, from which the signal of the pores needed to be extracted from the bulk signal. These indirect measurements and the fact that those semi one-dimensional samples were not isolated from the bulk, made interpretations not always easy and increase the uncertainty of the results.

In another branch of our physics community, namely optics, they started to produce photonic crystal fibers (PCF) [98] [99]. The PCF also known under the terms: holey fiber, hole-assisted fiber, microstructure fiber, or micro structured fiber, is an optical fiber which obtains its waveguide properties from an arrangement of very tiny and closely spaced air holes, which go through the whole length of fiber. These holes were made from larger capillaries of which, with stacking tube techniques, kilometer long capillaries could be produced with roughly equal holes (diameter) sizes over the whole length.

As in time the diameters of the holes (started in high micrometer regime) reduced, it became an interesting size for us when the group of Russell [100] was able to enter the nanometer regime [5]. It was the first time that long cylinders with inner diameters of ~ 540 nm could be made. Picture 4.5(a) shows a SEM [6] imagine of the cross-section of the fiber as received by the manufacturer. Here we see the channels in the fiber surrounded by a coating with a total diameter of 100 μm. In total every fiber has 324 channels, which are arranged in a honeycomb structure spaced ~ 1 μm from each other. Their diameters vary between 250 to 950 nm, see the distribution function of the diameters in figure 4.6. Except of the holes at the corners of the honeycomb structure, the channels look very circular, see figure 4.5(c) for a close up. Also the axial direction of the channel, see cut through of the fiber in figure 4.5(d), looks very smooth and continuous on the resolution of the SEM (for more details about the roughness, see section 4.3.1).

[5] Initially the group of Russell provided us this fiber. Later on the procedure was commercialized and produced by a company in Denmark: Crystal Fibre A/S [101].

[6] All the SEM images were scanned by the FEI Nova 200 NanoSEM.

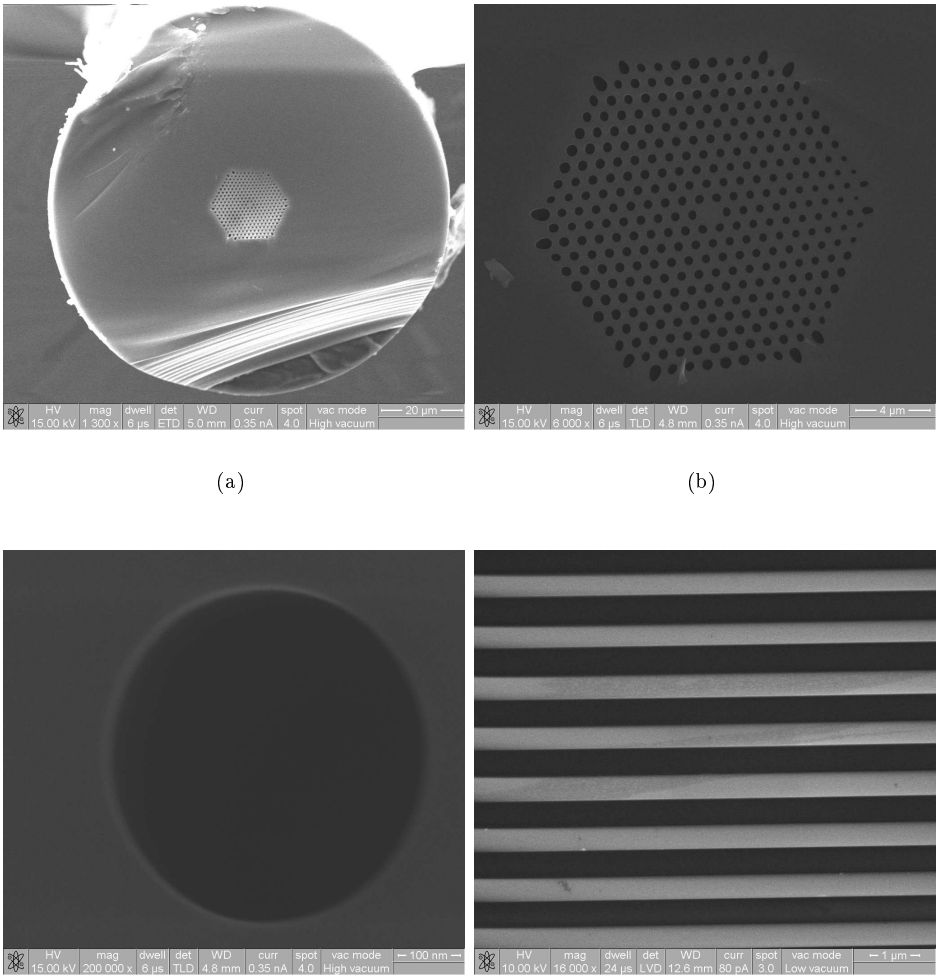

(a) (b)

(c) (d)

Figure 4.5: SEM images of the photonic crystal fiber, SEM images were scanned with the FEI Nova 200 NanoSEM. (a) Cross-section of the fiber, the total diameter (including glass coating) is 100 μm. The central core is 20 μm. (b) Zoom of the central core. Here the 324 channels are arranged in a honeycomb structure, with a distance of 1 μm between them. The diameter of the channel is around 540 nm. (c) Cross-Section of one channel. The image looks very circular, for which the channels can be considered very cylindrical. (d) Cut through along the axis of the fiber; on the resolution scale of the SEM the channels look very straight without variation in the diameter.

According to the SEM results, it is clear that the channels in the fiber are very

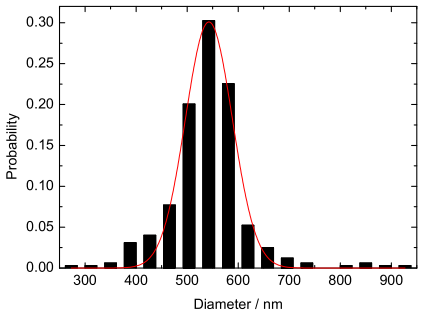

Figure 4.6: Distribution of diameters of the channels in one fiber. The distribution is fitted with a Gaussian (red line). The mean μ is 543 nm and the standard deviation σ is around 46 nm.

cylindrical. However, as is shown in figure 4.6 there is some distribution in the diameter of these channels. Desirable is that the standard deviation is as small as possible, but we are limited by the production process of these fibers. The mean μ (diameter) of the channels is 543 nm, with a standard deviation (σ) of 46 nm. As one will expect certain kinks in the resonance frequency shifts in the NMR spectrum (this will be described in the following sections), the distribution in the diameters will smoothen out these kink effects.

A more important issue is that one needs enough ^{3}He atoms to detect any NMR signal. As one can see from figure 4.5(a), the coating of such fiber is (relatively) enormous, which will result in a very low filling factor for the NMR experiment. The first concern was to etch as much coating as possible. The coating is made of quartz glass (SiO_2), which can be etched by hydrofluoric (HF) etching. The etching and the procedure was as follows:

- The photonic crystal fibers (PCFs) were cut into pieces of approximated 7.5 cm.
- Both ends of the PCFs were closed by the stycast 1260, were the capillary action sucks the stycast into the channels for maximally 5 mm.
- Fibers were etched with HF solution (HF:H_2O=10:1) for 30 minutes. Outside diameter of the PCFs was reduced to 30 μm. The stycast at the ends of fibers prevented any etching inside the channels.
- Etched PCFs were cleaned intensively with distilled water.
- The PCFs were dried in oven for 30 minutes at 100 °C.
- Ends of the PCFs were cut for 5 mm to remove the nanochannels filled with stycast 1260.

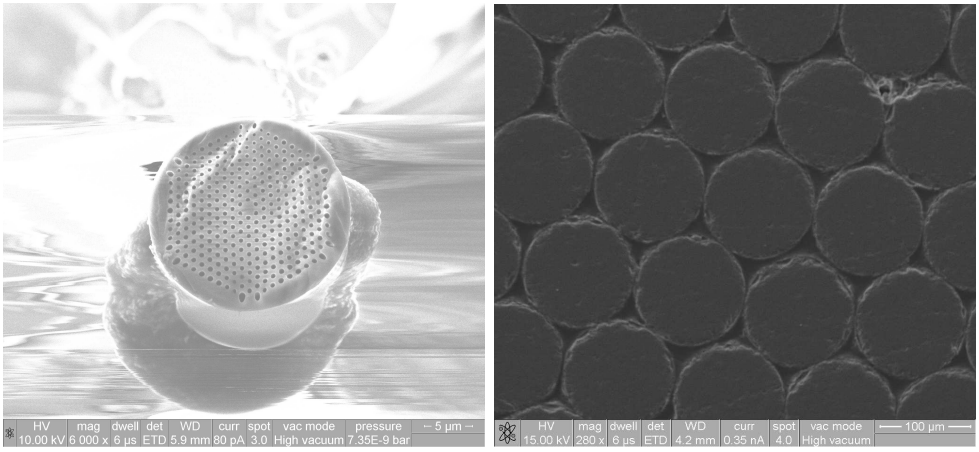

(a) (b)

Figure 4.7: (a) Photonic crystal fibers after HF etching. In this particular case the diameter is reduced from 100 to 20 μm. (b) Bundle of fibers glued together with stycast 1260, the packed could be made so tied that is close to honeycomb structure.

The etching decreases the outside diameter significantly, as can be seen in figure 4.7(a). To increase the filling factor for the NMR experiments these fibers were bundled to getter. This bundle is formed inside a PEI cylinder with inner diameter of 1 mm (Figure 2.1, the red part). The procedure was as follows:

- The PCFs were cleaned in pure CH_3OH (methanol) under ultrasonic vibration, in the same time all of PCFs were sunk into the PEI cylinder. As the etching increases the static charge on the fibers, the methanol helped to shuffle them into the PEI cylinder.
- To evaporate all the CH_3OH (in the channels and between the PCFs) the PEI capillary was put in an oven for 24 hours at 100 °C.
- To fill the spaces between the fibers some drops of stycast 1260 were put on the PCFs in the PEI capillary. Again the capillary action sucks maximally 5 mm into the nanochannels. However, the rest of the stycast was, due to the surface tension forces, sucked into the spaces between fibers.
- The bundle was dried at room temperature for 24 hours, after that another full day in the oven at 70 °C.
- Both ends of the bundle were cut for 5 mm and examined in SEM. The results showed that the nanochannels were opened and distributed (close to) in honey-

comb structure, see figure 4.7(b). No open space was visible between the fibers or between the fibers and the surface of the PEI cylinder.

- Flow rates were measured (with helium and leak detector) to confirm the total cross-section of the channels of the bundle.
- Place (glue) the PEI (including bundle of fibers) in the experimental cell (see figure 2.1), and close the top part of the bundle with stycast 1260.
- Final leak tests were done at liquid nitrogen and liquid helium temperatures.

Despite the effort to put as many channels (fibers) together, the total volume is still very small. The total volume of the channels is around 1.5 % compared to the empty PEI cylinder with inner diameter of 1 mm. Then the total amount of ^{3}He atoms which we could detect with our NMR probes should be around 1.4 μmole. This amount, in combination with our weak coupling read-out system (see section 2.4), should be sufficient to get NMR signals with sufficient SNR at our desirable magnetic field ($\mathbf{B}_0$) and bandwidth.

4.3.1 Roughness

The roughness of the channels is important to know how diffuse or how close one is to the specular boundary conditions. The SEM images already exposed that the roughness of these channels is smaller than the resolution of the SEM ($\sim$ 5 nm), and for better resolution the surface roughness measurements were performed with an atomic force microscope (AFM). A method was invented to cleave the PCF along the axis without damaging the surface structure inside the nanochannels, allowing us to characterize the morphology of the nanochannels in the PCF. A multi-wall carbon nanotube (MWCNT) mounted at a commercial AFM probe and a super sharp silicon tip were used to characterize the wall roughness in the nanochannels.

Introduction

In order to perform roughness measurements one should first consider two key problems: how to describe a rough surface accurately and how to detect and measure a rough surface. A (close to) random rough surface can be described mathematically. If a surface roughness can be described by a (Gaussian) random process, then the statistical parameters describing the surface height variation can be completely defined based on its height distribution and autocorrelation function, that is, the surface is totally determined in a statistical sense. A lot of work has been done to derive surface roughness descriptions that can be practically used for both one dimensional ($1D$) and two dimensional ($2D$) situations [102], [103], [104], [105], [106], [107], [108]. Gaussian distributions have been experimentally shown to be valid for many engineering surfaces [108]. An alternative assumption is that the autocorrelation function has an exponential form, which has also been verified experimentally [104], [105], [106]. It is well known that both height parameters and spatial functions are needed to describe the height distribution and textures of rough surfaces [109]. Autocorrelation function and autocorrelation length (λ_0) have been widely used in surface-related studies [110], [111], [112], [113], [114] to provide spatial information in addition to amplitude parameters, such as root mean square (RMS) roughness.

The mathematical tools used for the analysis of a random rough surface, which can be described mathematically as $z = z(x, y)$, where z is the surface height of a rough surface with respect to a smooth reference surface defined by a mean surface height and $\mathbf{r}$ is the position vector on the surface. One of the main characteristics of a random rough surface is the distribution function (one dimensional distribution function), $p(z)$. The meaning of $p(z)$ is that the probability of a surface height between z and $z + dz$ at any point on the surface is $p(z)dz$. The distribution $p(z)$ is a non-negative function of z and is normalized such that

$$\int_{-\infty}^{\infty} p(z)dz = 1. \tag{4.10}$$

The height distribution function provides a complete specification of the random variable $z(\mathbf{r})$ at a position $\mathbf{r} = \mathbf{r}(x, y)$. Although different rough surfaces may have different height distributions, the most generally used height distribution is the Gaussian

height distribution,

$$p(z) = \frac{1}{\sqrt{2\pi\sigma^2}} e^{-\frac{z^2}{2\sigma^2}}, \tag{4.11}$$

due to its mathematical simplicity and its place in the central limit theorem of the sum of large amount of random variables, where σ is the RMS deviation. The σ describes the fluctuations of surface heights around an average surface height. Larger σ means a rougher surface, under the condition that other roughness parameters stay the same. Sometimes the average roughness σ_{avg} is used to describe surface roughness and is defined as the arithmetic average of height z,

$$\sigma_{avg} = \int_{-\infty}^{\infty} |z - \bar{z}| p(z) dz. \tag{4.12}$$

Usually people do not consider higher-order moments, because the 1^{st} order moment $\bar{z}$ and the 2^{nd} order moment σ^2 are sufficient to characterize surface roughness for most purposes. However, higher order moments can give more information about the surface height distribution, and sometimes one needs higher order moments to differentiate the surface in more detail. The most important higher order moments are the 3^{rd} and 4^{th} order moments. The third order moment defines the skewness of surface height S_{sk},

$$S_{sk} = \frac{1}{\sigma^3} \int_{-\infty}^{\infty} z^3 p(z) dz. \tag{4.13}$$

Note that the S_{sk} is dimensionless in contrast to the RMS roughness, which is in units per length. The 4^{th} order moment defines the kurtosis of surface height S_{ku},

$$S_{ku} = \frac{1}{\sigma^4} \int_{-\infty}^{\infty} z^4 p(z) dz. \tag{4.14}$$

Kurtosis is also a dimensionless quantity.

The height distribution function only describes the statistical properties of random variables of a random field at individual positions. Different rough surfaces can have the same height distribution $p(z)$ and σ. In order to differentiate the spatial differences, one needs to know the connection of the random field $z(\mathbf{r})$ at positions $\mathbf{r}_1$ and $\mathbf{r}_2$. To do that, the joint distribution probability density function $p_j(z_1, z_2; \mathbf{r}_1, \mathbf{r}_2)$ of $[z(\mathbf{r}_1), z(\mathbf{r}_2)]$ is introduced, and it satisfies:

$$\int_{-\infty}^{\infty} \int_{-\infty}^{\infty} p_j(z_1, z_2; \mathbf{r}_1, \mathbf{r}_2) dz_1 dz_2 = 1, \tag{4.15}$$

$$\int_{-\infty}^{\infty} p_j(z_1, z_2; \mathbf{r}_1, \mathbf{r}_2) dz_1 = p(z_2), \tag{4.16}$$

$$\int_{-\infty}^{\infty} p_j(z_1, z_2; \mathbf{r}_1, \mathbf{r}_2) dz_2 = p(z_1), \tag{4.17}$$

where $p(z_1)$ and $p(z_2)$ are called the marginal distribution of $p_j(z_1, z_2; \mathbf{r}_1, \mathbf{r}_2)$, and for a homogeneous random field, $p(z_1) = p(z_2) = p(z)$. In general, $p_j(z_1, z_2; \mathbf{r}_1, \mathbf{r}_2)$ is not only related to the height distribution, but also to the correlation of heights between two separated positions.

The most important statistical characteristic of a joint distribution $p_j(z_1, z_2; \mathbf{r}_1, \mathbf{r}_2)$ is the auto-covariance function,

$$G(\mathbf{r}_1, \mathbf{r}_2) = \int_{-\infty}^{\infty} \int_{-\infty}^{\infty} z_1 z_2 p_j(z_1, z_2; \mathbf{r}_1, \mathbf{r}_2) dz_1 dz_2, \tag{4.18}$$

or the autocorrelation function,

$$R(\mathbf{r}_1, \mathbf{r}_2) = \frac{G(\mathbf{r}_1, \mathbf{r}_2)}{\sigma^2}. \tag{4.19}$$

For homogeneous isotropic rough surfaces we consider $G(\mathbf{r}_1, \mathbf{r}_2)$ and $R(\mathbf{r}_1, \mathbf{r}_2)$ only depending of the distance between $\mathbf{r}_1$ and $\mathbf{r}_2$, hence

$$G(\mathbf{r}_1, \mathbf{r}_2) = G(\mid \mathbf{r}_1 - \mathbf{r}_2 \mid) = G(\rho), \tag{4.20}$$

and

$$R(\mathbf{r}_1, \mathbf{r}_2) = R(\rho), \tag{4.21}$$

where, $\rho = \mid \mathbf{r}_1 - \mathbf{r}_2 \mid$. The quantity is the translation and sometimes is called a lag. The autocorrelation function $R(\lambda)$ has the following properties:

- $R(0) = 1$
- $R(-\lambda) = R(\lambda)$
- $\mid R(\lambda) \mid \leq R(0)$
- $z(r)$ and $z(r + \lambda)$ are independent from each other for the limit $\lambda \to \infty$; for the limit for $\lambda \to \infty$ $R(\lambda) = 0$

The autocorrelation length λ_0 of an autocorrelation function is usually defined as the value of the lag length at which the autocorrelation function drops to $1/e$ of its value with respect to zero lag, i.e. $R(\lambda_0) = 1/e$. For a random rough surface, the information of the correlation functional represents a good description of surface morphology.

Preparation

In order to open the channels along the axis of the fiber, the fiber was glued into the holder, see figure 4.8(a). The whole holder was immersed in liquid nitrogen, and after thermalisation the holder was quickly taken to room. The difference in thermal expansion between the grey Araldite and metal and the predefined groove breaks the cylinder along the axis. This result made it possible to perform AFM and SEM measurements on the inside of the fiber.

As the open PCF samples are not (relatively) flat (curvature of the cylinder), conventional commercial silicon nitride AFM tips would not be suitable. These tips are too wide compared to their length, and for this reason would not be suitable to obtain a good profile from inside the channels. This concern made us use two different kind of AFM tips, the super sharp silicon tip and multi-wall carbon nanotube tip. Both are relatively long compared to their width, and their results are compared with each other. The used atomic force microscopy was the: Nanoscopy III Multimode AFM, Digital Instruments/Veeco Instruments. The AFM measurements were performed in contact and/or the non-contact/tapping mode.

The super sharp silicon non-contact/tapping mode AFM probe [115] is shown in figure 4.8(b). The tips have a high aspect ratio, its radius of curvature is 2 nm, the half cone angle at 200 nm from the apex is smaller than 10°, and the typical aspect ratio at 200 nm from the tip apex is of the order 4:1. As shown in the Figure 4.8(b), the length from the apex of the tip to the point with a radius less than 100 nm and is longer than 400 nm, so that the apex of the tip can reach to the bottom of the channel.

The used multi-wall carbon-nanotube (MWCNT) AFM tip was home made by the group of Frenken, Oosterkamp and Rost [116]. First the multiwall carbon nanotube must be placed on the end of silicon AFM tip by using a custom-built nanomanipulator assembly inside a scanning electron microscope (FEI Nova 200 NanoSEM). This method allows retrieving a single MWCNT from an electrode covered with MWCNTs and attached (by gold coating), see figure 4.8(c), to a commercial AFM probe (Olympus AC240TS, nominal resonant frequency 80 kHz, sputter coated with 5 nm of Molybdenum-Germanium followed by 70 nm of Gold). The fabricated multiwall carbon nanotube AFM probe, see figure 4.8(d), had a length of 320 nm, and a diameter of 30 nm with an apex less than 5 nm.

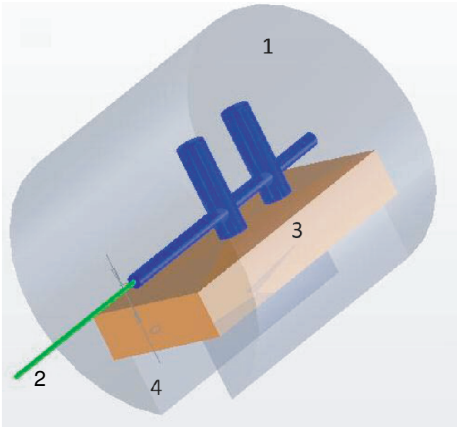

(a) Holder to break the cleaved fiber along the axis of photonic crystal fiber. (1) Grey araldite. (2) Position to cleave the photonic crystal fiber by thermal expansion. (3) Metal bar. (4) Pre-crack groove.

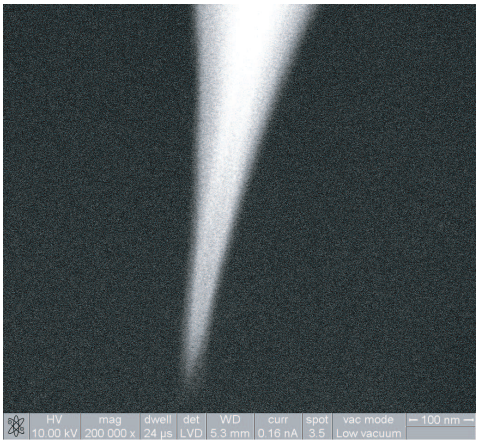

(b) Super Sharp Silicon Noncontact Tapping mode - High Resonance Frequency Commercial atomic force microscope probe.

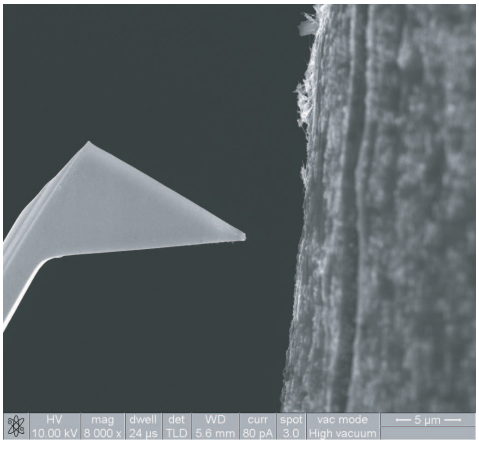

(c) Mounting multi-wall carbon nanotube on the top of the AFM probe.

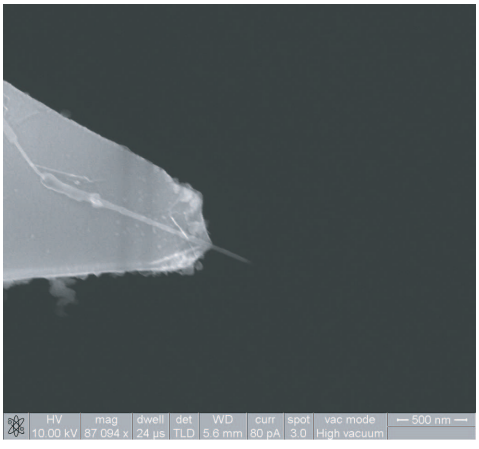

(d) Homemade AFM carbon nanotube probe used for visualization and characterization of channel wall roughness of the photonic crystal fiber.

Figure 4.8:

Results and discussion

Atomic force microscopy (AFM) made it possible to create high resolution images of non-conductive surfaces. In contact AFM a cantilevered probe is slid over the surface of the sample. The deflection of the cantilever is a measure of the force working on the probe. A laser beam bounces from the back of the cantilever to a photodiode enabling the determination of the deflection while a piezo moves the sample under the tip so that it slides over the surface. Contact mode is mostly done using silicon nitride tips. In tapping mode AFM the cantilevered probe oscillates close to its resonant frequency tapping the surface with the probe at the lowest point of the oscillation. The oscillation of the cantilever is monitored while a piezo moves the sample under this oscillating probe. A feedback loop ensures that the oscillation of the cantilever is kept constant and thereby the tapping force. The resolution of the AFM is 0.1 to 0.2 nm laterally, and 0.1 nm vertically.

An example of the AFM image, which mapped the whole curvature of the channel, is shown in picture 4.9. However, as we are interesting to find the roughness and correlation lengths of such a channel, scan sizes this size are not suitable for analysis. First of all, while both tips have the right shape to scan at the bottom of these channels, it can give problems when we scan close to the edges. Secondly, step sizes of the AFM are digitally controlled. The step sizes are determined by a 2 × 12 bit system [7] (for the X and Y direction), meaning that long scan ranges will increase the step sizes. This can obscure the interpretation of the roughness of the channel, and/or can miss the existence of a (short) coherence length. For these two reasons scans are made in the middle of the channel, and are kept relatively small (100 to 200 nm) in one direction (perpendicular to the axis of the channel). The scan direction along the axis of the channel was varied between 100 to 1600 nm, so that any coherence length at different length scales can be studied.

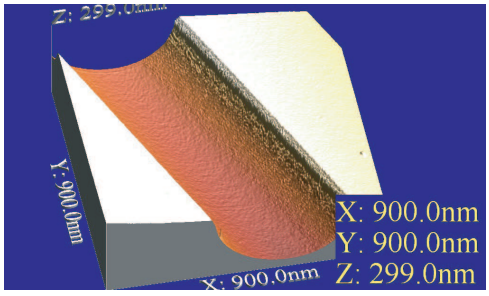

Figure 4.9: AFM images measured by a silicon super sharp tip. Scan size of 900 × 900 nm^2.

[7] The XY position is constructed by 512 × 512 matrix (9 bits in each direction). Leaving 3 bits for the Z coordinate.

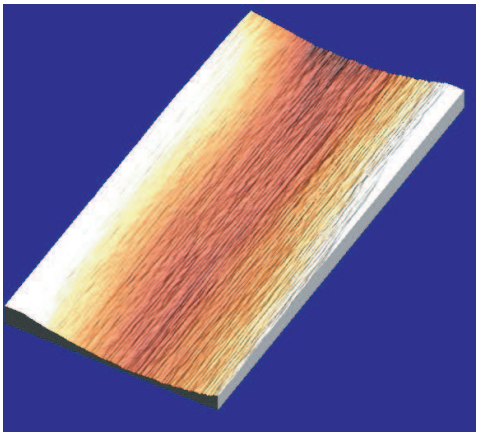

(a) Example of an AFM image of the inside of a photonic crystal fiber with a silicon super sharp tip. Scan size is 200x100 nm^2.

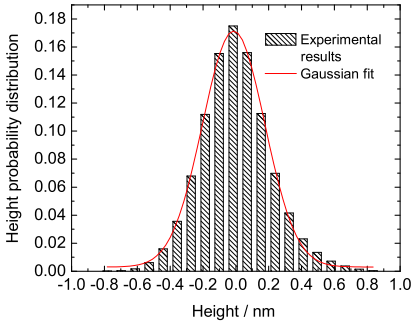

(b) Height probability distribution function made of one of the surface profiles taken from figure 4.10(a).

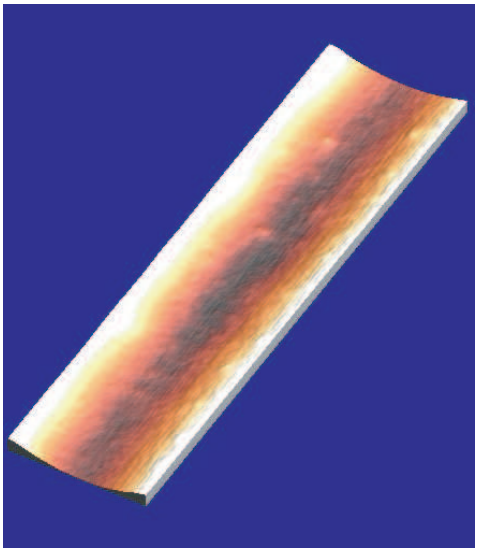

(c) Example of an AFM image of the inside of the photonic crystal fiber with a multi-wall carbon nanotube tip. Scan size is 800x200 nm^2.

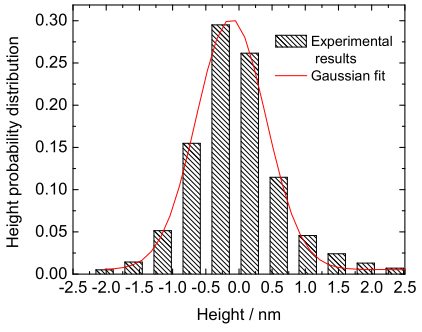

(d) Height probability distribution function made of one of the surface profiles taken from figure 4.10(c).

Figure 4.10:

Probe type	Scan size nm × nm	2σ nm	$2\sigma_{avg}$ nm	S_{ku}	S_{sk}	λ_0 nm
Multi-wall carbon nanotube tip	1600 × 200	0.95	0.61	22.90	2.88	25.76
	800 × 200	0.89	0.63	10.61	1.84	22.88
	400 × 200	0.73	0.52	5.75	0.57	23.76
	200 × 200	0.62	0.43	5.67	0.56	12.69
Super Sharp Silicon tip	100 × 100	0.82	0.56	8.16	-1.56	2.95
	200 × 50	0.75	0.56	4.89	0.37	16.14
	200 × 100	0.34	0.26	4.80	0.31	12.91
	200 × 200	0.86	0.65	8.70	0.22	16.27
	800 × 100	0.81	0.62	4.91	0.64	26.76

Table 4.3: Statistical roughness parameters of the channels, for different scan ranges and AFM tips.

Typical results of AFM scans of both tips are plotted in figure 4.10 together with one of the height probability distribution functions corresponding with the surface profiles, which are represented by a Gaussian. For both tips and all different scan ranges the statistical parameters are obtained according to equations (4.11), (4.12), (4.13), (4.14), (4.18) and (4.19). The acquired parameters are listed in table 4.3, and are averaged from several measurements at different places from the same sample. Comparing the parameters we observed that the amplitude of the roughness (σ) in all cases is smaller than 0.5 nm. As one can already see by eye in figures 4.10(b) and 4.10(d) the height distribution has a Gaussian form, meaning that the roughness is close to a homogenous (random) distribution. This is confirmed by the value of the kurtosis S_{ku}, a perfect random surface has an S_{ku} of 3. Our values are still reasonable close to that number, however as they are larger than 3, it indicates a leptokurtic distribution (more peaked than a normal distribution). This is also seen back in the skewness S_{sk}, which should be zero in the case of a perfect Gaussian distribution function. While the values of the parameter are relatively close to zero, they are almost all positive which indicates (again) to peakness in the channel. However, it is questionable if the roughness is really more peaked than dipped. Reasonable is to believe that it can be a feature of the measurement. Namely, it is always harder for a tip to reach the bottom of a valley than the top. Nevertheless, we consider our channels pretty homogenous with a roughness amplitude smaller than 0.5 nm, as is shown by the performed measurements of all scan sizes, and this result seems independent of the used tip.

Another phenomenon observed in the measured data, which is most probably not a real feature, is that for the longer scan ranges the kurtosis and skewness seem to increase. The feedback mechanism works in all circumstances (scan sizes) with the same speed, meaning that for longer scan ranges the feedback gets relatively slower. This was problematic for the super sharp silicon tip, often the tip broke

as the feedback could not prevent touching/smashing [8] the tip into the surface, the reason why the longest scan sizes are not be performed with this tip. As the multi-wall carbon nanotube is a bit smaller and less fragile, longer scan sizes could be performed, however the problems in the feedback mechanism for such 'long' scans were the same. This made us believe that some artificial results are crept in our data for the longer scan sizes. On the other hand it should be mentioned that significantly less scans are made on these scales (once more because of the difficulties it brings with them), for which the error in the (average) value is also higher.

Concerning the correlation length λ_0, one should realize that some curious features with regard to the autocorrelations function for finite samples can occur. As is pointed out by the authors Ogilvy and Foster [117]: The full exponential height correlation function of a surface profile will only be measured if the sampling interval is less than one tenth of the correlation length λ_0, and for best rough surface statistics the ratio of surface extent to correlation length must be 60 (or bigger). This is in our case not trivial, as we are always wrestling with the sample interval vs. total scan length. However, our correlation functions, from which we obtained the correlation length, have an exponential behavior. So the acquired (average) coherence length λ_0, as is put in table 4.3, are obtained by exponential fits. From here it seems that the coherence lengths get longer for increasing scan lengths [9], which is an indication that we did not scan over long enough distances to extrapolate the real size of the coherence length from the data. However, when we put all data in one graph, see figure 4.11, the coherence length seems to approach a plateau for long enough scan ranges. The phenomenon that one comes closer [10] to the 'real' coherence length of a system by increasing the scan lengths is known, and for example well described in the book of Meakin [118]. The used fit function, the exponential growth [11], is given by

$$\lambda_0(x) = -26.49 \exp(0.0038x) + 26.49. \tag{4.22}$$

The data of both tips seem to correspond which each other, and it seems to approach the value close to 26.5 nm. The longest scan range is already close to this value, and as the scan conditions [12] are very close to the condition as determine by Ogilvy and Foster, it is an extra indication that this may indeed be a the 'real' value of the coherence length in the channels. This coherence length is most likely induced by the method of production of these fibers and the surface tension of SiO_2. If any coherence

[8] Except of position problems, the feedback could also bring the tip in oscillation introducing obscure results in the measurements.

[9] Correlations lengths are search in the directions along the channel axis.

[10] In the situation one starts with scan sizes which are not long enough to preview to 'real' coherence length.

[11] The preference of an exponential growth seems reasonable concerning the behavior of the data, which is supported by the theoretical explanation that such scaling is linear on log-log scales.

[12] If one assume that the coherence length of 26.5 nm is a 'real' coherence length in our system, then our scan size is more than 60 times the coherence length in case we scan 1600 nm. Also the interval is $1600/512 = 3.125$, which is very close to the one tenth of correlation length ($3.125/26.5 \approx 0.12$). It means that we are very close to the condition to observe the coherence length of the system.

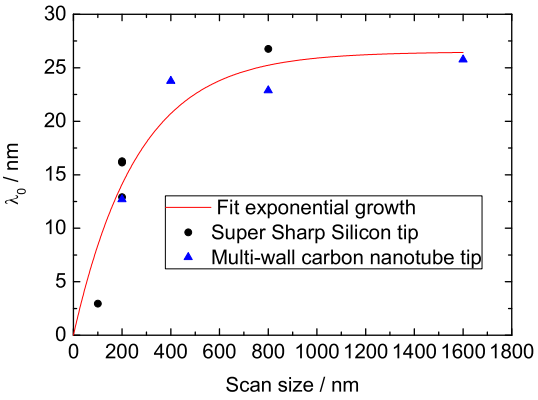

Figure 4.11: Correlation lengths λ_0 as founded by the autocorrelation function as function of scan size. Black circles are correlation lengths obtained from the data with super sharp tips, the blue triangles are obtained with the multi-wall carbon nanotube. Data could be fitted with an exponential growth, and seems to approach a maximal correlation length of 26.49 nm.

at longer scales is present in our systems, then those values will not be detected with our used techniques (limitation of scan size).

Interesting is that both tips describe more or less the same statistical parameters. As all measurements are a deconvolution between tip and sample, it makes the information about the channel more reliable as it is confirmed by two different kinds of tips. It is also, by our knowledge, the first time that roughness measurements are performed on the holes inside the photonic crystal fibers.

4.4 Expected NMR 'fingerprint' in narrow cylinders

4.4.1 A-phase

For educational purposes first the resonance frequency shifts in the bulk A-phase are described. One can derive these shifts in an equivalent way to what was done for the B-phase in section 3.2. The full derivation we will omit, because the results are perfectly described in Leggett's paper [21], from which we quote the solutions of (3.3) as:

$$\Omega_{xx}^2 = 0, \tag{4.23}$$

$$\Omega_{yy}^2 = \Omega_{zz}^2 = \frac{6}{5}\frac{\gamma^2}{\chi_A} g_D(T) \equiv \Omega_A^2. \tag{4.24}$$

The A-phase is very interesting in that it has a *transverse* resonant frequency shift:

$$(\omega_\perp^A)^2 = \omega_L^2 + \Omega_A^2, \tag{4.25}$$

and a *longitudinal* resonant frequency [13]:

$$\omega_\parallel^A = \Omega_A. \tag{4.26}$$

The (transverse) resonance frequency shift was already observed [35] before the theoretical understanding, and actually started the intensive theoretical studies to anisotropic susceptibility of superfluids.

In the bulk A-phase [14] the dipole energy is minimized when the preferred direction in spin space $\hat{\mathbf{d}}$ is perpendicular to the magnetic field [15] $\mathbf{B}_0$ (the magnet field of the NMR magnet), but aligned with $\hat{\mathbf{l}}$. The vectors $\hat{\mathbf{l}}$ and $\hat{\mathbf{d}}$ parallel or anti-parallel is referred as dipole-locked, for which (4.25) is the solution. The more general solution, valid for the dipole unlocked regions due to surface and/or topological defects, is given by [22]:

$$\omega = \omega_L + \frac{\Omega_A^2}{2\omega_L}\cos(2\Theta(\mathbf{r})), \tag{4.27}$$

with $\Theta(\mathbf{r})$ the angle between the $\hat{\mathbf{l}}$ and $\hat{\mathbf{d}}$ vector.

4.4.2 Polar-phase

As in the polar-phase the orbital space $\hat{\mathbf{w}}$ and spin space $\hat{\mathbf{d}}$ have only one preferred direction, and in absence of any spin-orbit interaction the vectors do not need to be in any fixed relative configuration to minimize the energy, the dipole energy does not lift the degeneracy [119]. Consequently the $\hat{\mathbf{w}}$- and $\hat{\mathbf{d}}$-vector can be parallel or perpendicular or have any other configuration.

Any relative orientation may not be energetically favorable, but as shown by [21] and [120], determines whether the superfluid NMR signal has a longitudinal or transverse frequency component. In the case that the vectors $\hat{\mathbf{w}}$ and $\hat{\mathbf{d}}$ are aligned parallel there is no transverse resonance frequency shift, but a longitudinal resonance can be found at the frequency of

[13] Strictly spoken these solutions are only valid in the so called high field limit, $\mathbf{B}_0 \gg 3$ mT, which is fulfilled in a general NMR experiment.

[14] As the A-phase is not mentioned in this thesis before: The preferred direction in spin space $\hat{\mathbf{d}}$ and orbital space $\hat{\mathbf{l}}$ are macroscopically ordered independent from each other, this in contrast with the B-phase where the orientation is relative from each other. However, in the case of a pure A-phase (without surface effects and magnetic fields) the dipole energy is minimized if both vectors $\hat{\mathbf{d}}$ and $\hat{\mathbf{l}}$ are parallel.

[15] Technically this would be the A_2-Phase. Here $\Delta_+ > \Delta_-$, but the dipole energy is still minimized if $\hat{\mathbf{d}}$ is along the $\hat{\mathbf{l}}$-vector.

$$\omega_{\parallel}^2 = 2\Omega_A^2. \tag{4.28}$$

Here the longitudinal frequency is expressed in the longitudinal frequency component of the A-phase.

In the case that $\hat{\mathbf{w}}$ and $\hat{\mathbf{d}}$ are perpendicular, there should be no longitudinal resonance. However, a transverse resonance frequency shift is expected, behaving as:

$$\omega_{\perp}^2 = \omega_L^2 + 2\Omega_A^2. \tag{4.29}$$

If one compares this with equation (4.25), a shift twice the shift in the bulk A-phase is expected. So, the longitudinal or transverse frequency components are determined by the relative orientation of $\hat{\mathbf{w}}$ and $\hat{\mathbf{d}}$, and in general one can say that the longitudinal and transverse resonance frequencies are given by:

$$\omega_{\parallel}^2 = 2\Omega_A^2 \cos^2\gamma \tag{4.30}$$

$$\omega_{\perp}^2 = \omega_L^2 + 2\Omega_A^2 \sin^2\gamma, \tag{4.31}$$

where γ is the angle between $\hat{\mathbf{w}}$ and $\hat{\mathbf{d}}$.

4.4.3 Axial state

If an A-phase-like-state (axial state) is realized in a confined geometry, one creates (as in the case of the B-phase) textures inside the container. In this case the boundary conditions require that the $\hat{\mathbf{l}}$-vector is perpendicular to the surface [89]. If the radius R of the cylinder fulfills the condition: $\xi(T) \ll R \ll \xi_D$, $\hat{\mathbf{l}}$ and $\hat{\mathbf{d}}$ are uncoupled [16]. A magnetic field parallel to the cylinder's axis will orient $\hat{\mathbf{d}}$ into the plane perpendicular [17]. In this situation the most likely textures are the Mermin-Ho (MH), radial- , and circular disgyration, see figure 4.12. In static conditions, for radii $R/\xi(T) \geq 10$ the MH-texture is stable.

For narrow cylinders with $R/\xi(T) < 10$, the disgyration-type of textures become the stable ones. This condition can be reached as well, since the coherence length is tunable with temperature and pressure. In general one can say that close to the transition temperature T_c [18] the radial disgyration has the lowest energy of the three textures [19].

As NMR potentially provides the best clarification which texture is present in the narrow channel, it is important to know how the frequency will shift. In the conditions of narrow cylinders, $\xi(T) \ll R \ll \xi_D$, then Takagi's prescription [122] yields for the longitudinal and transverse resonance frequencies:

$$\omega_{\parallel} = R_{\parallel}\Omega_A, \tag{4.32}$$

[16] If the dipole coherence length ξ_D is much longer than the radius R it can be considered as a dipole free situation, for which the vector $\hat{\mathbf{d}}$ can be considered uniform in the container.

[17] The reader is reminded that $\hat{\mathbf{d}}$ is perpendicular to the spin angular momentum of the cooper pairs $\mathbf{S}$; $\hat{\mathbf{d}} \cdot \mathbf{S} = 0$.

[18] Here the coherence length is relatively long, since $\xi(T) = \xi_0(1 - T/T_c)^{-1/2}$.

[19] As calculated in the dipole free situation.

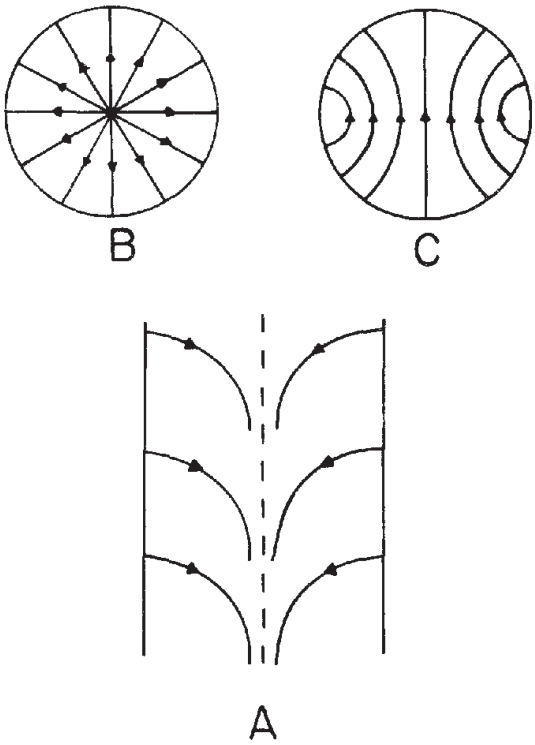

Figure 4.12: The three textures. The arrows indicate the $\hat{\mathbf{l}}$-vector direction. (A) Side view of the MH-texture; (B,C) top views of the radial- and circular disgyration texture, respectively. Figure is taken from [121].

$$\omega_{\perp}^2 = \omega_0^2 + R_{\perp}^2 \Omega_A^2, \tag{4.33}$$

where $R_{\parallel}$ and $R_{\perp}$ are scaled frequency shifts for the longitudinal and transverse components, respectively. $R_{\parallel}$ and $R_{\perp}$ contain the (average) orientation of the $\hat{\mathbf{l}}$ components in the cylinder. In the local-oscillator model Bruinsma and Maki [121] calculated the frequency shifts of each texture for cylinders with a radius of 1 μm, the results are put in table 4.4. As the $\hat{\mathbf{l}}$ has cylindrical symmetry (around the axis of the cylinder) for the MH- and radial disgyration textures, one does not expect a longitudinal resonance mode. The transverse resonance shift comes from the (average) difference between the $\hat{\mathbf{l}}$ components in the plane perpendicular to the axis of the cylinder, hence $R_{\perp} = \sqrt{< l_x^2 > - < l_y^2 >}$.

On the other hand, as for example is shown by [123], if we have a sufficiently small ratio of R/ξ_0 [20], the radial disgyration texture is most favorable. Here the

[20]In the calculation of Bruinsma and Maki the ratio was around $R/\xi_0 \approx 50$. In ref [123] the ratio

	Mermin-Ho texture	Radial disgyration	Circular disgyration
$R_{\parallel}^2$	0	0	0.70
$R_{\perp}^2$	0.20	0.50	0.85

Table 4.4: $R_{\parallel}^2$ and $R_{\perp}^2$ as calculated by Bruinsma an Maki [121] for cylinders with a radius of 1 μm.

angle between the $\hat{\mathbf{l}}$- and $\hat{\mathbf{d}}$-vectors [21] rotates by 360 degrees when it goes around the center of the cylinder. In this configuration the regions $\hat{\mathbf{d}} \parallel \hat{\mathbf{l}}$ and $\hat{\mathbf{d}} \perp \hat{\mathbf{l}}$ are equal, see figure 4.12B. The region $\hat{\mathbf{d}} \parallel \hat{\mathbf{l}}$ will give a positive frequency shift $\omega_{\perp} = \sqrt{\omega_L^2 + \Omega^2}$ and the region $\hat{\mathbf{d}} \perp \hat{\mathbf{l}}$ will give a negative frequency shift $\omega_{\perp} = \sqrt{\omega_L^2 - \Omega^2}$. Here the two opposite shifts will cancel each other, which gives a net transverse resonance shift of zero. In other words, the scaled frequency shift $R_{\perp}$ has no net value, hence $R_{\perp} = \sqrt{< l_x^2 > - < l_y^2 >} = 0$. Of course also no longitudinal mode is expected here, as the $\hat{\mathbf{l}}$-vector has rotational symmetry around the axis of the cylinder.

One property of the axial state should be emphasized. This is an equal spin pairing state, for which the susceptibility should be constant (to first order) as function of temperature [12] [21] regardless of any frequency shift.

4.4.4 B-phase

As the coherence length decreases by lowering the temperature or increasing the pressure, see equations (1.33) and (1.34), the ratio between R/ξ increases. By enough reduction, meaning the ratio of R/ξ becomes significantly large (see figure 4.2), the container can be considered more like a bulk system. Concerning these narrow fibers, we do expect to see the (distorted) B-phase for low enough temperatures (or/and high enough pressure). Of course, as now $\xi_H \gg R$, the wall of the cylinder will play a dominating role in the distribution of the $\hat{\mathbf{n}}$-texture over the sample, as explained in sections 3.3 and 3.4.

It is not completely clear how the $\hat{\mathbf{n}}$-vector would behave in such small cylinders with $R \ll \xi_H$, but as shown in the case of diameters of 1 mm, see sections 3.8 and 3.9, it is most likely to act similarly to one of those textures. Meaning that, in the case the wall completely dominates the spatial distribution of the texture, the transverse NMR shift would behave as in equation (3.9) with $\beta = \cos^{-1}(1/\sqrt{5}) \approx 63.4°$. In the alternative configuration, the $\hat{\mathbf{n}}$-vector gradually changes from the boundary conditions at the wall to the boundary condition at the center of the cylinder, resulting

was considered to be $R/\xi_0 < 5$, which is energetically more favorable for the radial disgyration, and more applied to the conditions of our experiment, as our radius is around 270 nm and the coherence length ξ_0 around 50 nm.

[21] The $\hat{\mathbf{d}}$-vector is assumed to rotate rigidly in the presence of an external radio frequency field $\mathbf{B}_1$, and lies in the xy-plane.

in a broader NMR absorption line shape [22] (compared to the A- or normal phase), which coincides with $\beta(r)$ varying over the sample between zero and approximately 63.4°. In this case the NMR spectrum is given by equation (3.10).

In previous experiments the ratio between the amount of ^{3}He atoms at the surface and in the liquid was so small, that any (few) layer(s) of ^{3}He atoms adsorbed at the surface of the container's wall hardly had any influence on the obtained NMR signals. However, in this confined geometry the ratio between the atoms positioned at the surface/volume is around 1 ‰. Although the total number of adsorbed atoms may still be a small fraction of all the atoms in the channel, they do act as a solid layer, for which the Curie-Weiss susceptibility is considerable larger than that of the Fermi liquid, and cannot be ignored. The Curie-Weiss law is given by:

$$\chi = \frac{C}{T - \theta}, \tag{4.34}$$

where θ is the Curie-Weiss constant, which is around 0.5 mK for solid layers, see for example [124]. The constant C is referred to as the Curie constant and for spin $\frac{1}{2}$ systems is given by

$$C = \frac{\mu_0 N_A (\frac{1}{2}\gamma\hbar)^2}{k_B}, \tag{4.35}$$

where N_A is Avogadro's number.

It is known that there is a rapid exchange rate between the liquid ρ_1 and the solid ρ_2, and if one use magnetic resonance frequencies small compared to this exchange frequency a single NMR line will be observed [125]. As described by the paper of Hook and Kaplinsky [126] about the B-phase, in the absence of driving forces and dissipation, the spin angular momentum densities $\mathbf{S}_1$ and $\mathbf{S}_2$ of respectively the liquid and solid atoms satisfy [23]

$$\ddot{\mathbf{S}}_1 = \dot{\mathbf{S}}_1 \times \omega_L - \Omega^2 \cdot \sigma_1 - \rho_1 \dot{\mathbf{S}}_1 + \rho_2 \dot{\mathbf{S}}_2. \tag{4.36}$$

From here the NMR frequencies can be deducted and are given by

$$\omega_0^2 = \frac{1}{2}(\omega_L^2 + \mu\Omega_B^2) + \sqrt{\frac{1}{4}(\omega_L^2 + \mu\Omega_B^2)^2 - \omega_L^2 \mu\Omega_B^2 \cos^2\beta}, \tag{4.37}$$

this differs only from the bulk result by the substitution of $\mu\Omega_B^2$ for Ω_B^2 in equation (3.9). In the limit of $\mu\Omega_B^2 \ll \omega_L^2$ [24] equation (4.37) can be rewritten as

$$\omega_0 \approx \omega_L + \frac{\mu\Omega_B^2}{2\omega_L} \sin^2\beta, \tag{4.38}$$

[22] In this configuration we do not expect to see any spin waves. The radius of the cylinder is considerable smaller than in case of section 3.8, consequently the characteristic length L_1 of equation (3.32) is so small that the energy levels between of the spin wave modes will be so large that even the lowest spin wave mode cannot exist in such a confined geometry.

[23] Here the isotropic susceptibility of the B-phase is already taken into account. For derivation of the A-phase one should start from the more general expressions.

[24] As is the case in our experiments.

where $\mu = M_{liq}/(M_{liq} + M_{sol})$. M_{liq} and M_{sol} are the total magnetization of the liquid and solid, respectively (see also [127]).

Another important feature of the B-phase is that its susceptibility should decrease as is explained in section A.3.

4.5 NMR results of the channels

4.5.1 Normal state

The channels, to perform NMR on it, where installed at the position as is illustrated in the red part of figure 2.1. The ratio of the signal from the coil around the channels compared to the signal from the coil around the 1 mm cylinder (blue part of figure 2.1), of course in the same conditions (pressure and temperature) and in the normal state, was close to 0.01. This would indicate that the total cross sectional area of the ^{3}He in the fibers is 1 % of that in the cylinder, which is reasonably close to the estimated [25] 1.5 %. Upon cooling the observed susceptibility seems to saturate at 50 mK, as is expected in the Fermi liquid theory (FLT) (see section 1.1). Thus we confirmed that there is ^{3}He liquid [26] in the channels. Another indication is that the NMR signals [27] increased as function of pressure as expected in the FLT (densities get higher and more quasi-particles can be 'seen' in the same volume); the susceptibility should change as described by equations (1.5) and (1.6), which was in good agreement with the measurements.

Only a few measurements are performed on the ^{3}He in the fibers in the normal state, mainly in preparation for cooling to the lowest temperatures, nevertheless they did confirm that the channels were filled with liquid helium. This result by itself is already an achievement, and proved that our weakly coupled transformer technique is able to detect one μmole ^{3}He in low magnetic field (15 mT) with a bandwidth of 2.6 Hz.

4.5.2 Channels cooled down to the lowest temperatures

Initially the channels were filled with liquid ^{3}He near zero pressure, for which the coherence length is the longest (see table 4.1) and non-bulk superfluid properties would be more significant. However, even by cooling to the lowest available temperature (down to 100 μK) no transverse NMR shifts [28] were observed. Although it is possible

[25] In our estimation we assumed that average diameters of the channels were 540 nm, which is clearly not true as we can see from figure 4.6. However, as we are not sure that all used fibers have the same distribution in diameter, we used this average number. Surely, it would give an additional error, but as it is only to compare the order of magnitude, it should not be a problem.

[26] As for example the helium would have been solidified, we should have seen the Curie-Weiss behavior.

[27] If for some reason we mainly observed solid ^{3}He, we would hardly see any pressure dependency.

[28] The raw data did show a small shift. The reason is that still some straw field of the demagnetization magnetic is observed at the experimental setup and that the magnetization of the solid (adsorbed ^{3}He at the walls) is visible in these small channels. Both effects are noticeable far for any

that a phase transition to the axial and/or polar phase has occurred, as explained in section 4.4.2 and 4.4.3, since it is possible that these phases have no transverse resonance frequency shift, it is still remarkable that no (distorted) B-phase properties were visible at the lowest temperatures. It could be that the coherence length of the Cooper pairs is still too large compared to the diameter of the narrow channels (or too much diffuse scattering) to form a superfluid (at any temperature). For this reason we increased the coherence length (by increasing the pressure), but never a transverse resonance frequency shift was observed. Eventually the pressure was increased [29] to 10 bar, which reduced the coherence length more than twice, see table 4.1. Nevertheless, we did not observe any shifts, not to mention any observation of a transition to the B-phase.

The observed signals were obtained at the original position of the rf-coil in figure 2.1, or as pointed out in detail in figure 4.14(a). An example of the absorption signal is plotted in 4.13(a), which is an average of 238 measurements at 10 bar near 500 μK.

T_c (Bulk), and after subtraction of both effects no net shift was observed.

[29] We did not dare to go higher in pressure, as we were afraid that the glued parts will not hold it, and eventually would explode our cell.

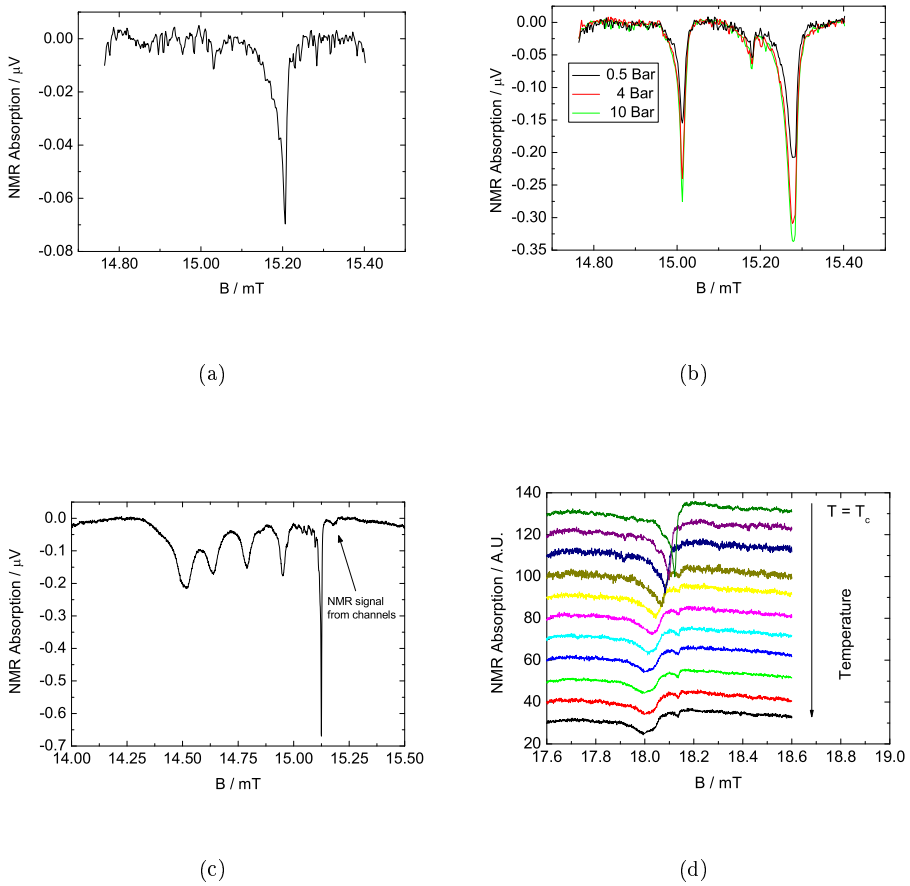

Figure 4.13: (a) NMR signal of the ^{3}He in the channels, with the tank coil positioned as illustrated in figure 4.14(a). Here the ^{3}He is at 10 bar and 500 μK and the signal is averaged over 238 sweeps. This signal consists of a single absorption line which does not show any transverse resonance frequency shift at any temperature. (b) NMR signal of the ^{3}He in the channels, with the tank coil positioned as illustrated in figure 4.14(b). Here the data is plotted for 0.5, 4 and 10 bar, where the temperature is just above the bulk T_c corresponding to that pressure. The small middle peak corresponds to the ^{3}He inside the channels, the two side peaks most likely originate from the ^{3}He in the open spaces between the fibers. We treat this in detail in section 4.5.4. (c) NMR signal of the ^{3}He in the channels and in the 1 mm cylinder, with the tank coil positioned as is illustrated in figure 4.14(c). The temperature is around 300 μK and the pressure is 6 bar, while the signal is averaged 52 times. In the total line shape we see the existence of spin waves in the cylinder part, and the remaining part (at the Larmor frequency) is believed to be the signal from the channels. (d) NMR signal of ^{3}He in the channels immersed in 'bulk' ^{3}He as illustrated in figure 4.14(d). The 'bulk' part undergoes a phase transition into the B-phase (at the expected T_c). The part of the line shape from the ^{3}He in the channels stayed in resonance at the Larmor frequency, for the whole temperature range. Here data is shown for 2.1 bar (typically averaged for 80 times) at temperatures between $0.4T_c$ and T_c. Resonances are here at higher magnetic fields (Larmor frequency coincides with 18.12 mT) as the used tank circuit had a resonance frequency of 588 kHz.

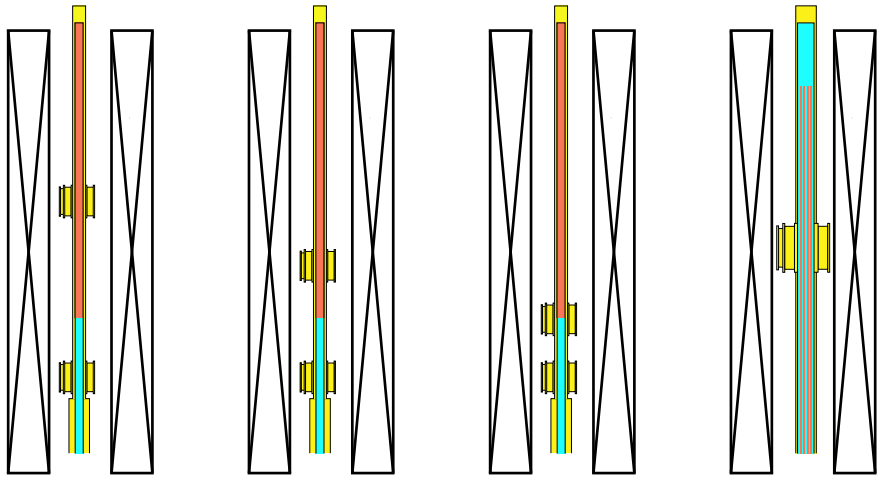

Figure 4.14: The various configurations of the experimental setup, showing the different positions of the tank coil around the channels relative to the interface of the bulk liquid in the 1 mm cylinder.

Since the behavior of the observed signals in the channels in configuration 4.14(a) contradicted our expectation and the physical intuition, we considered the possibility that spurious heat released from the quartz glass and the stycast 1260 (still stored and/or created due to NMR) was sufficient to prevent the liquid in the channels to cool below the critical temperature. While this was estimated [30] to be not the case, we wanted to corroborate this by reducing half the distance between the coil position and the interface between channels and the 1 mm cylinder, as illustrated in figure 4.14(b). The NMR result of this configuration is plotted in figure 4.13(b)

[30] All heat created/stored in quartz/PEI (This will be discussed in more detail in the following paragraphs of this section), which wants to be released in the ^{3}He of the channel should overcome the Kapitza resistance between the liquid helium and the SiO_2. This Kapitza resistance is determined by the acoustic mismatch theory, which describes the boundary resistance as: $R_K = \triangle T/\dot{Q} = 15\hbar^3\rho_s v_s^3/(2\pi^2 k_B^4 T^3 A \rho_h v_h)$. The resistance was calculated for 1 mK, for which the density of ^{3}He $\rho_h = 0.082$ g cm^{-3} and the sound velocity is 194 m s^{-1} [128]. The total estimated surface area of all the channels was 40 cm^2. The quartz has a density of $\rho_s = 2.66$ g cm^{-3} and a sound speed of $v_s = 5570$ m s^{-1}. This will give a 'Kapitza conductance' of $\dot{Q}/\triangle T \approx 8.3 \cdot 10^{-11}$ W K^{-1}. This should be compared to the thermal conductance through the ^{3}He in the channels, using the thermal conductivity κ of ^{3}He at 1 mK, $\kappa \approx 2$ mW cm^{-1} K^{-1} [31]; and as the fibers are roughly 6.5 cm long, the thermal conductance through the channels filled with helium could be calculated to be $\dot{Q}/\triangle T = -\kappa\ A\ /\triangle x \approx 2.5 \cdot 10^{-8}$ W K^{-1}. If the heat transferred over the Kapitza resistance has any significant influence on temperature of ^{3}He inside the channels, then the conductances should have the same order of magnitude, meaning that the temperature gradient over the Kapitza resistance should be 3 orders of magnitude higher than over the ends of the channels. It is not likely that such an high temperature is build up in the cylinder, as the thermal radiation would not allow such high temperatures on the outside of the cell and for such high gradients the thermal conductivity (κ of quartz is $1 \cdot 10^{-5}$ W cm^{-1} K^{-1} at 50 mK) through the glass/PEI down to the experimental space is better than over the Kapitza resistance.

(still in the normal state), which has the most remarkable feature that we observe 3 absorption lines instead of one. We believe that the two peaks away from the Larmor frequency originate from unclosed spaces between the fibers (somehow the stycast was not able to fill all the spaces there), the middle peak fits the right frequency/field and amplitude to correspond to the ^{3}He in the channels. When the liquid is cooled below T_c the two side peaks seems to undergo a phase transition, which we will describe in detail in section 4.5.4. In the remaining part of this section we will focus ourselves on the signal coming from the channels only.

As the ^{3}He in the channels are positioned closer to the interface between fibers and cylinder, and one consider the heat release from the quartz to liquid helium a problem, then the temperature gradient (from interface to position of tank coil) should definitely be smaller compared to the initial situation. However, when we repeated the measurement [31], as in the case of the initial measurements, no transverse resonance frequency shifts were observed (or change in the susceptibility).

As these results correspond to the previous measurements, we were willing to put the tank coil even closer to the interface. As a matter of fact we put the tank coil at the position [32] of the interface, which is illustrated in figure 4.14(c). In this position the signal is observed from both the channels and the cylinder, and in the normal state no difference between the signals can be made as they both overlap at the Larmor frequency [33]. As we cool down from this position, the spin waves in the cylinder are created as explained in chapter 3, and as all modes of this spin waves shift away from the Larmor frequency, it is possible to separate the two signals. In figure 4.13(c) the NMR results at the interface are shown at a temperature of approximately 300 μK and 6 bar; the results are averaged 52 times. Here it is believed that the remaining absorption line at the Larmor frequency is the signal from the channels. This believe becomes stronger as the total ratio between the absorption signals is (approximately) proportional to the volumes and taking into account that the susceptibility of the ^{3}He inside the cylinder is reduced by a factor $\frac{1}{3}$. As the temperature gradient between the inside of the channels and the interface should now be rather small, it is curious that even in this conditions (300 μK and 6 bar) no transverse resonance frequency is observed, and hard to believe that the temperature (inside the channels) is too high to form the B-phase.

[31] Again from zero to 10 bar.

[32] Actually only 1.5 mm of the tank coil was put over the channels and the rest over the cylinder.

[33] The side peaks as observed in figure 4.13(b) can be observed as they are far enough from the Larmor frequency, and their amplitude is roughly a factor two smaller compared to the previous position.

If sufficient heat was generated in the quartz or the stycast due to the rf-field (which is unlikely [34]) or stored heat was released over time [35], one can imagine that it will influence the thermal equilibrium too much. However, these heat sources were considered to be too small to be harmful. Nevertheless, it was decided (by the lack of any evidence of a B-phase transition) to analyze NMR results of unglued fibers. Meaning that we have still a PEI cylinder full of these fibers, but without any stycast (enormous reduction of hydrogen in the system, plus no direct contact between fibers and PEI). This PEI cylinder had a 2 mm inside diameter, in which the fibers are 'freely' spaced. The total volume of channels compared to the volumes between the fibers was estimated to be 15 %. As the spaces between the fibers are relatively large, the ^{3}He should behave nearly as in bulk, meaning that it will undergo the normal $\rightarrow$ B-phase transition. An overview of this configuration can be seen in figure 4.14(d). Results of the measurements on this cell are plotted in figure 4.13(d). Here the pressure was 2.1 bar, and the was cooled below 0.4 T_c. Below T_c we see that the 'bulk' liquid undergoes the phase transition to the B-phase, the susceptibility reduces an $\hat{\mathbf{n}}$-texture is formed. Consequently, the resonance frequency shifts [36] away from the Larmor frequency. For low enough temperatures we can distinguish the remaining absorption peak at the Larmor frequency. This signal correspond to the 15 % (volume ratio) compared to the bulk signal in the normal phase. We are convinced [37] that the signal is from the liquid in the channels. Again we observe the familiar result that the signal in the channel seems to be unchanged as function of temperature (or pressure). Here a significant part of the hydrogen atoms are removed and is surrounded by liquid ^{3}He, for which the heat can be drained off much better. Again

[34] Heat is of course generated (other sources than in the ^{3}He) due to NMR measurements in the stycast/PEI, mostly because of the hydrogen in the polymer. However, the experimental sweeping scans are around the magnetic fields corresponding to the resonance frequencies of ^{3}He, for which the hydrogen tail is far away (see for example figure 2.18). Technically oxygen and silicon (from the quartz glass) do have isotopes with a net nuclear spin, however their natural abundance is small 0.038 % and 4.6832 %, respectively. Besides, their tails (as they are further away) are even smaller, for which the total heat generated by those spin is considerable smaller. The heat generated in the hydrogen (around the channels and for used sweeps values) was estimated 3 times more than in the ^{3}He inside the channels, where the total generated power was calculated to be $1 \cdot 10^{-16}$ W. To estimate the upper limit of a temperature gradient created in these channels, we assumed that all heat was released into the top of the channels. The thermal conductivity κ in ^{3}He at 1 mK is about 2 mW cm^{-1} K^{-1} [31], and as the fibers were roughly 6.5 cm long, the thermal heat transported through the channels filled with helium could be calculated by $\dot{Q} = -\kappa\ A\ \triangle T/\triangle x$. The estimation showed that an incredibly small gradient $\triangle T$ of 4 nK is needed to conduct all this heat, which seems to be practically unharmful for the experiment.

[35] These problems are known as for example is notified by Pobell [31]. However, the heat releases are small and are approximately 0.1 nW g^{-1} at 1 K, and decrease exponentially over time. This half life time may be around a day, which is relatively short compared to the total time the dilution fridge was performing at the lowest temperatures (weeks, sometimes months). Hence these heat releases should be negligible overtime, if not already from the start. Also no differences over time are seen.

[36] As the geometry of this cell, cylinder filled with 'free' fibers, is rather complicated, we did not put much effort to understand what kind of textures will be formed, or how that will shift the NMR frequency. Of course it is intuitively understandable that the $\hat{\mathbf{n}}$-vector will bend over the sample, which will coincide with a shift in the transverse resonance frequency (see equation (3.9)).

[37] An other candidate will be adsorbed/solid ^{3}He, however the signal is considered to be too large, and one should expect to see an increase of the susceptibility, as it has an Curie-Weiss behavior.

it seems that the heating concerning the hydrogen atoms is of no influence on the effects we observe. The only heating source, which cannot be eliminated, is the quartz glass itself. However, as all heat, created or released, due to the SiO_2 in the quartz glass was estimated much smaller than in the case of the hydrogen atoms, we considered it to be unlikely to warm up the liquid to a significant level.

4.5.3 Discussion

As is reported in the previous section, no NMR shifts are observed of the ^{3}He inside the channels. One may think that it is reasonable to assume that the liquid is still in the normal state and no phase transition has occurred at all. If the liquid is still in the normal state, it can be of two reasons.

- The suppression of the superfluid transition in these geometries is much stronger than theoretically is calculated. The phase diagrams as calculated by Li and Ho, see figures 4.4(a) and 4.4(b), are for cylinders with a radius [38] of 300 nm. Additional suppression should than be more than a *millikelvin*, a scenario which seems to be unlikely.

- Another scenario can be that the liquid inside the channels is not cooled into the submillikelvin regime. The test of several different configurations, to reduce temperature gradients and heat sources, did not show any changes in the NMR results. This is unexpected as the temperature gradient of some configuration (especially at the interface) should be nil. Also heat transport calculations showed that the liquid inside the channels should have been cooled into the submillikelvin regime, overall an unlikely scenario as well.

At this point it should be emphasized that we have never observed a transition into the B-phase. However, we cannot exclude that a phase transition has happened. The B-phase should have been the easiest to detect, even without any shift in the resonance frequency, because the susceptibility should decrease. One important remark should be made about earlier measurements in slab geometries. Freeman and Richardson [129] also never observed the A-B phase boundary in their 300 nm slab geometry, which is also in contrast with theoretical calculations, see for example [130, 86]. It may be that the absence of the B-phase has the same basis for both geometries, and that for unknown reasons the theoretical calculations are too optimistic. Only when slab geometries become bigger, for example by Bennett *et al.* [91], the A-B phase boundary is observed. In this particular case the slab geometry is around 600 nm.

For the polar or any axial states, which are equal spin pairing states, we do not expect (at least till second order) changes in the susceptibility. We will now discuss their expected resonance frequency shifts for our geometry.

Axial states If any axial state would have been formed then, as explained in section 4.4.3, calculations showed that no net resonance frequency shift for small cylinders

[38] Our average radius is around 270 nm, which is close enough to expect similar phase diagrams.

should occur. Small is here considered when $R/\xi_0 < 5$ [39], which is definitely the case in most conditions of our experiments. Only for the highest pressures we do not fulfill this criteria, maximally the ratio was $R/\xi_0 \approx 10$, however even for these ratio's the most likely texture must be the radial digyration [40] for which the net transverse resonance frequency shifts will be zero. So, if we would have had an axial state in our channels it would have been unnoticed by our transverse NMR experiment. Longitudinal experiments are also not suitable for clarification of this state, as the symmetrical symmetry of the $\hat{\mathbf{l}}$-vector in the radial disgyration texture will not have any net components for longitudinal NMR shifts either.

Polar states The NMR shifts of the polar state are determined by the angle γ between the vectors $\hat{\mathbf{w}}$ and $\hat{\mathbf{d}}$, as described in section 4.4.2. Concerning our geometry, we would expected that the $\hat{\mathbf{d}}$-vector is perpendicular to the axis of the cylinder (magnetic field is parallel to the axis of the cylinder), and that $\hat{\mathbf{w}}$ is perpendicular to the wall [41] of the cylinder. In this case we would only have a longitudinal frequency shift. It should be mentioned that Takagi said [123], concerning the B-phase in confined pore geometry, the symmetry axis of the orbital components is parallel to the magnetic field, which is a consequence that some components of the order parameter are suppressed at the wall of the B-phase (leaving the Polar phase). It is this possibility we had taken into consideration. If this configuration would be realized, then it is not the longitudinal component which will be measured, but the transverse resonance frequency shift.

Reasons to perform transverse NMR experiments around the channels were to unravel how the relative orientation of the $\hat{\mathbf{w}}$ and $\hat{\mathbf{l}}$-vector was configured in such a small cylinder. It would also be a good method to observe if any characteristic time scale (T_1 or T_2) would change in this superfluid. Also, as is pointed out by Barton and Moore, the phase transitions could be 1^{st} and 2^{nd} order, which could be clarified by hysteresis experiments.

However, the observation of the B-phase failed to occur, and by the lack of this orientation point made the performing of the above ideas hard. The problem now is that the existent of the two others states can not be excluded/included by our performed experiments. It means that our cell configuration should have serious modifications to prove if any of these states exist inside the channels. The following points should definitely be considered:

- Experiments at higher pressures: The cell should be strengthened so that experiments at higher pressures can be performed. Initially the use of low pressures was desirable, as here the coherence length ξ_0 is the largest and non-bulk properties would have been expected for these conditions. However, the lack of

[39] The calculations of Takagi [123] were done in this regime.

[40] Energy calculations excluding superfluid mass and spin currents showed that the radial disgyration texture should be the most stable one if $R \leq 10/\xi(T)$.

[41] As in the case of the $\hat{\mathbf{l}}$-vector in the axial state.

observing any B-phase transition makes it desirable to even decrease the coherence length more. As this coincided with increasing pressure, one should be sure that the cell should be able to withstand it.

- The possibility to perform longitudinal NMR: This can be accomplished when an oscillating field is applied along the external magnetic field. In this configuration the $\hat{\mathbf{d}}$-vector tends to rotate (at resonance) in the plane normal to the magnetic field, which will be observed by the probe. However, this experiment is far from trivial [42], and is definitely not easy as the expectation of the polar state only exist in a small fraction of the phase diagram, see figures 4.2, 4.4(a) and 4.4(b).

- Perform an experiment with an angle γ between the cylinder axis and the externally applied magnetic field. This is presumably a better alternative than the longitudinal experiment. If we have an angle γ (say 45°), we will create both a finite transverse and longitudinal component, in case we deal with the polar phase. Here the transverse component is easier to detect than the longitudinal component. The axial state will probably be a bit harder to interpret in this condition, and it should be re-estimated/recalculated which shifts can be expected. Also the bore of the magnet should be increased, to be able to make a configuration with large enough angle between the magnetic field and the cylinders axis.

- Heat transport measurement through the channels: This method should help to probe the gap structure of the superfluid, possible allowing to reconstruct the phase. However, this method cannot determine the symmetry of the order parameter.

- Torsional oscillator: Alternative method to determine if any mass decouples from the system, a method to indicate if any superfluid is formed in the channels.

At least in this stage it cannot be said with any certainty if a superfluid or not is formed inside the channels. It should be emphasized that experiments in real long cylinders with diameters of a few times the coherence length were never performed before. There is still the possibility that a deeper physical cause excludes a (quasi) one-dimensional superfluid [43]. However, there are some cautious and reserve claims that the polar phase has (indirectly) been seen in small pores and aerogel, see for instance [131] and [96]. Even if the polar phase really existed in these confined geometries it is not with the same boundary conditions. The (average) radial direction may be of

[42] To quote D.D. Osheroff about his longitudinal experiments in the A-phase [10]: *"I searched hard and long for such a mode, but found nothing. In the end, I gave up the idea that the mode would be sharp, and assumed instead that it would be very broad. In this case, one could not detect it by sweeping the NMR frequency, since one would then sweep over the broad Q of the NMR tank circuit. I decided to hold the frequency fixed and sweep the temperature, thereby sweeping the longitudinal resonance through my probe frequency. This strategy worked quite well, and the resonance was very broad."*

[43] Compare one dimensional crystals, where (quantum) fluctuations are not damped by the lack of long range order and make these crystals unstable.

the same order, but the axial direction is small. As these geometries are surrounded by bulk liquid, it may be that the superfluid state inside such a pore is influenced by the bulk superfluid B-phase (proximity effect).

4.5.4 NMR shifts influenced by the adsorbed helium-3 at the wall

As already mentioned in section 4.5.2, the NMR signals, as we position the tank coil closer to the interface, reveal two additional absorption lines, see figure 4.13(b). It is clear that the signal cannot originate from the ^{3}He inside the channels, as their amplitude is too large and these absorption peaks are not observed for distances far enough from the interface [44]. However, we definitely observe two additional peaks, of which the resonance frequencies do not overlap with the ^{3}He inside the channels or themselves. One can imagine that some spaces between the fibers or between the fibers and the PEI wall are not totally filled with stycast, which would leave some open spaces that will be filled with liquid ^{3}He.

As it is believed that the additional signals (absorption lines) are coming from open spaces between the fibers and/or fibers and the PEI wall, it is strange that all those signals do not overlap, as the gyromagnetic ratio for all ^{3}He atoms is the same. Differences in magnetic fields of the order of the inhomogeneity ($\triangle H(\mathbf{r})/H = 5.4 \cdot 10^{-4}$) would somehow be helpful to explain this phenomenon. However, even then the signal should be a broad absorption line and not concentrated around three different resonance frequencies. In addition the difference between the two outer peaks is around 0.27 mT [45], which is over an order of magnitude more than the inhomogeneity of the magnet. Another interpretation could be that locally the solid (adsorbed helium at the walls) gives, due to its magnetization, a slightly different field. However, as the magnetization is approximately proportional to $1/T$, see equation (4.34), the absolute distance between the absorption lines should change as the temperatures is swept. If we compare our NMR signals from 100 mK to T_c ($\sim$ 1 mK), we do not see any change in the (magnetic) separation of the peaks, from which we exclude any solid to be the source of the magnetization. The only differences in separation we have observed were when we compared the data of different runs [46]. The differences were always small, but maximally an additional separation of 0.026 mT was observed between the furthest peaks. It is clear that the ^{3}He atoms, corresponding to each peak, must locally experience a different magnetic field (as function of $\mathbf{B}_0$), and as any additional magnetization/magnetic field or inhomogeneity of the magnet failed to explain it, we wondered if the magnetic field lines are homogenously distributed in the cell. If for any reason the magnetic field lines are not completely homogenously distributed,

[44] If ^{3}He enters the channels, they should fill the whole length of the channels.

[45] If one compares this with the chemical - or Knight shift, caused by the electrons that locally deform the magnetic field, is typically 1 ppm compared to the Larmor frequency. In our case the shift is $1 \cdot 10^{-2}$, which is (relatively) huge.

[46] In the same run, which means the period the cryostat was cooled (below 4 K) till it was warmed up, no changes in separations were observed even not if the cell was pressurized to different pressures.

but may have preferences for spaces with certain solid/liquid [47] ratios, then it would explain why certain volumes 'see' slightly different fields. Nevertheless, it cannot be said that this feature is understood at all, especially because of the largeness of the separation between the absorption lines.

While the phenomenon of having three separated peaks for the ^{3}He atoms is unexplained, it is very convenient since their isolation allows a careful study of each of them. The absorption spectrum above T_c is illustrated in figure 4.13(b). We know, as explained in section 4.5.2, that the middle peak is from the atoms in the channels. The two outer absorption lines, which we will call from now on the left and right peak (corresponding with the lowest and the highest current in figure 4.13(b), respectively), are suggested to correspond with ^{3}He in the open spaces between the fibers and fibers/PEI. The most important difference between these open spaces is the liquid to solid (adsorbed of ^{3}He at the wall) ratio. Taken into account how the fibers are bundled, we know that possible open spaces will have a kind of axial symmetry for which the radial direction can have a width (if completely open) of a few micrometers. These open spaces are perfect to study [48] the behavior of the B-phase for these dimensions. It is a bit surprising for the author, that not much data is published for cylindrical structures corresponding with these sizes *at low pressures.*

An example of what is observed in our NMR spectrum when we cooled the liquid below T_c, is plotted in figure 4.15. Here the pressure was 4 bar and the results are presented as if the liquid is cooling [49] from 1.39 mK (is T_c) to 0.64 mK. Once more it is illustrated that the middle peak (signal in channels) does not show any shift or reduction in the amplitude (susceptibility). The other two peaks undergo a phase transition [50] from the normal to the B-phase, both at the same temperature and at the bulk T_c (it must be said that any small suppression would not be detected as the temperature sweep rate (0.31 mK h^{-1}) was too fast for it). For both absorption signals, a reduction of the susceptibility is measured, characteristic for the B-phase. Also the absorption peaks get wider, as the $\hat{\mathbf{n}}$-vector bends over the sample. It results in an (average) frequency shift to the left, as is explained in chapter 3 and section 4.4.4. The right peak seems to move roughly 1.5 times faster than the left peak, and for low enough temperatures it even shifts through the Larmor line of the ^{3}He inside the channels. Eventually the absorption lines get very broad, which makes the SNR very small, and practically (with our used bandwidth) unable to follow anymore.

If one analyze the frequency shift, it is noticed that the shift is less than indicated by equation (3.9), because in this configuration the rapid exchange between the solid and liquid atoms cannot be neglected. As we wanted to determine the ratio between solid/liquid we should know the value of the μ parameter in equation (4.38), and

[47] The adsorbed ^{3}He atoms at the wall are 1 or 2 atomic layers thick, which can be (in average) slightly different in every run, and would be a possible explanation for different separations for certain runs.

[48] At least in our configuration where the absorption lines are clearly distinguishable. Would they have overlapped, it would become very unclear.

[49] Actually, for better thermal equilibrium, the data is obtained by heating the liquid.

[50] Well there was never really doubt about it, but this phase transition ones more proves that the absorption signals were also coming from ^{3}He atoms.

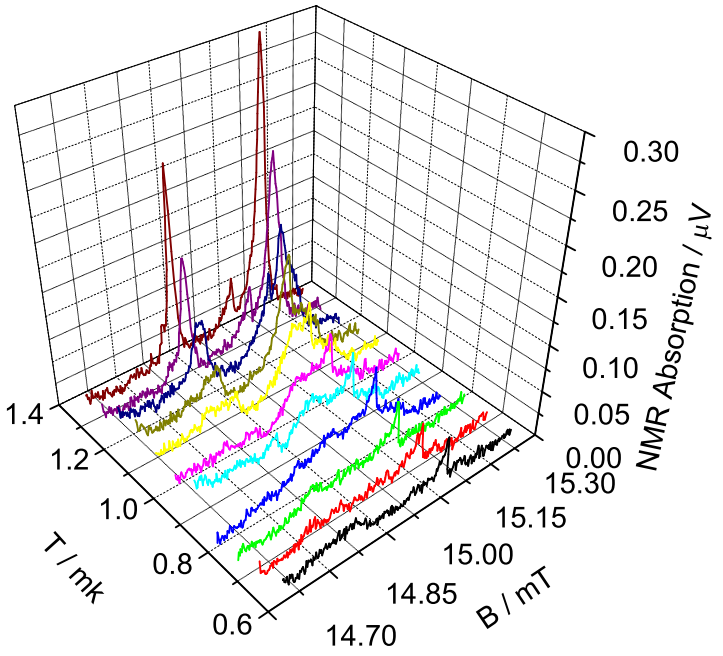

Figure 4.15: NMR absorption scans of ^{3}He as observed in the configuration of figure 4.14(b) at 4 bar, for various temperatures. The absorption is expressed in μV, which is the signal measured with the pick-up coil. The temperature range is between 0.64 mK and T_c (1.39 mK). At the transition temperature the 3 absorption peaks are in resonance at the Larmor frequency. The left and right absorption peaks come from the helium atoms in open spaces/pores between the fibers, the middle peak is the signal obtained from the atoms inside the channels. Lower temperatures show that the left and right peaks undergo a transition from the normal to the B-phase. The liquid inside the channels does not show any frequency shift or reduction of the susceptibility.

as the magnetization is proportional to susceptibility and field ($M = \chi H$), we can express μ in terms of susceptibilities, see equations (1.5), (1.6) [51], (4.34) and (4.35), where we should also take into account that the susceptibility of the B-phase χ_B is temperature dependent, as is described in appendix A.3.

[51]This equation is expressed in CGS units, and should be converted to SI units by multiplying with the permeability μ_0. Not to be confused with the magnetic moment.

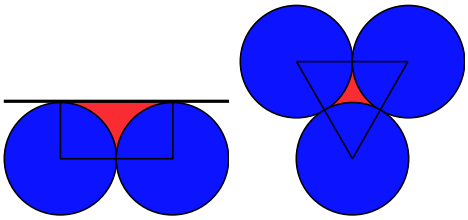

(a) (b)

Figure 4.16: An ideal cross section of the possible open space between our fibers. In both pictures the blue circles are the cross section of the fibers (the channels inside the fibers are not illustrated), which have approximately a diameter of 30 μm. The red area indicates the possible open space, due to the packing op the fibers. (a) The fibers against the (PEI) wall. Here the curvature of the wall is neglected as the diameter of the fibers is much smaller than the circumference of the PEI cylinder. The open spaces are in this configuration formed between the wall and the fibers. (b) Here the fibers are packed in a honeycomb structure, which leaves room for possible open spaces.

$$\mu = \left(1 + \frac{n_{sol}}{V_{liq}} \frac{N_A}{N_F} \frac{(1+F_0^a)}{k_B(T-\theta)} \left(\frac{\chi_B(T)}{\chi_N}\right)^{-1}\right)^{-1}, \tag{4.39}$$

Here n_{sol} is the amount (in mole) of atoms adsorbed to the wall, and V_{liq} the volume of the liquid. This formula has only two fit parameters, namely the ratio n_{sol}/V_{liq} and θ. The other parameters are constants, pressure or temperature dependent, but all theoretically known (see appendices). The parameter θ is known to be close to 0.5 mK, but if necessary the exact value can be obtained by fitting the data. We like to start by estimating the fit parameter n_{sol}/V_{liq}. The possible open spaces in our cell are considered to be between the honeycomb spaced fibers, and between the fibers and the wall (PEI), for which a sketch is illustrated in figure 4.16.

Given these ideal geometries, the open space (area) can be calculated. The amount of adsorbed ^{3}He atoms at the wall (the solid) must be estimated. We do know that only the first two layers will be immobile [52] and will be considered to form a triangular lattice [53] with an atom to atom distance of approximately 3 ångström.

[52] Only the first two layers experience an effective pressure (potential) higher than at melting curve.

[53] This is an assumption and mostly determined by the surface structure. Good atomically flat substrates have shown a hexagonal lattice for the solid layer. This is in our situation clearly not the case as the fibers are etched, but effectively we will assume a close packed hexagonal structure.

Open space between fibers and wall. The area is equal to the rectangle, as illustrated in 4.16(a), subtracted by two times a quarter of a circle.

$$A_{liq} = (A_{\square} - 2 \cdot 1/4 \cdot A_{\circ}) = (2r \cdot r - 2 \cdot 1/4 \cdot \pi r^2) \approx 96.57 \cdot 10^{-12} \text{ m}^2.$$

V_{liq} is the area times the length, hence $V_{liq} = A_{liq} \cdot l$.

The amount of atoms N at the surface of this open space, where we assumed that the atoms per layer form a regular arrangement with the highest packing coefficient [54](hexagonal packing), is given by:

$$\begin{aligned} N =& A_{wall} \cdot (highest\ packing\ coefficient)/(cross\ section\ one\ atom) \cdot (layers) \\ &= (2 \cdot 1/4 \cdot 2\pi r + 2r) \cdot l \cdot \frac{\pi}{2\sqrt{3}}/(\pi \cdot (1.5 \cdot 10^{-10})^2) \cdot 2 \approx 1.98 \cdot 10^{15}\ l. \end{aligned}$$

The ratio of n_{sol}/V_{liq} is now given by:

$$\frac{n_{sol}}{V_{liq}} = \frac{N/N_A}{V_{liq}} = \frac{1.98 \cdot 10^{15}\ l/(6.022 \cdot 10^{23})}{96.57 \cdot 10^{-12}\ l} \approx 34.03 \text{ mole m}^{-3}$$

Open space between fibers. The area is equal to the equilateral triangle, as illustrated in 4.16(b), subtracted by three times a sixth of a circle.

$$A_{liq} = (A_{\triangle} - 3 \cdot 1/6 \cdot A_{\circ}) = 1/2 \cdot 2 \cdot \sqrt{3} \cdot r^2 - 3 \cdot 1/6 \cdot \pi r^2 \approx 36.46 \cdot 10^{-12} \text{ m}^2.$$

Again the volume V_{liq} is the area times the length, hence $V_{liq} = A_{liq} \cdot l$.

The amount of atoms N at the surface of this open space is

$$\begin{aligned} N =& A_{wall} \cdot (highest\ packing\ coefficient)/(cross\ section\ one\ atom) \cdot (layers) \\ &= (3 \cdot 1/6 \cdot 2\pi r) \cdot l \cdot \frac{\pi}{2\sqrt{3}}/(\pi \cdot (1.5 \cdot 10^{-10})^2) \cdot 2 \approx 1.21 \cdot 10^{15}\ l. \end{aligned}$$

The ratio of n_{sol}/V_{liq} is now given by:

$$\frac{n_{sol}}{V_{liq}} = \frac{N/N_A}{V_{liq}} = \frac{1.21 \cdot 10^{15}\ l/(6.022 \cdot 10^{23})}{36.46 \cdot 10^{-12}\ l} \approx 55.07 \text{ mole m}^{-3}$$

From this calculation it is clear that the ratio n_{sol}/V_{liq} is different for the two types of open spaces, and smallest for the open spaces between the fibers and the wall. The solid magnetization has than less effect on the NMR shift of the B-phase, and as the shift of the right peak of figure 4.15 is less restrained than the left peak, it is reasonable to accept that the right peak corresponds to the open spaces between fibers and wall, and the left peak to the open spaces between the fibers.

[54]C.F Gauss proved that this packing coefficient for (2 dimensional) arrangement of circles is $\frac{\pi}{2\sqrt{3}}$.

If we want to fit the data with equation (4.38), it is convenient to know which line segment correspond to which β. As described in chapter 3 the $\hat{\mathbf{n}}$-vector will bend over the whole sample, for which we showed detailed calculations of the bending of the $\hat{\mathbf{n}}$-vector in a cylindrical geometry. In our open spaces the bending of the $\hat{\mathbf{n}}$-vector is clearly observed as well, as the width of the left and the right peak of figure 4.15 get broader for lower temperatures. Calculations of the bending of the vector considering these geometries are far from trivial, and are for this reason omitted. However, the sizes of the open spaces are relatively small compared to the magnetic healing length ξ_H, for which we (as again explained in section 3.3) expected that the $\hat{\mathbf{n}}$-vector will not be completely bent between the two boundary conditions ($\beta(0) = 0$; $\beta(R) = 63.4°$), but mostly determined by the boundary conditions at the wall ($\beta = 63.4°$), as this should be the most energetically favorable state for dimensions ($\sim$ 10 μm) much smaller than the magnetic healing length ($\xi_H \sim$ 1 mm).

If we inspect the observed shifts in more detail, we do observe that the mean of the line shape asymmetrically moves away from the Larmor frequency, which is illustrated in figure 4.17, which forms a 2D projection of figure 4.15. Not only does the absorption peak becomes broader, as expected as the angle between the $\hat{\mathbf{n}}$-vector and the magnetic field varies over the sample, but becomes also asymmetric with the minimum of this absorption line being positioned at the left side. This means that in most part of the sample the $\hat{\mathbf{n}}$-vector has an angle with the magnetic field corresponding to this line segment, and as this minimum is most left of the broadened absorption line, it seems reasonable to believe that it corresponds to the maximal achievable angle, which is 63.4°. This idea is strengthened by the realization that for these narrow cylinders (small compared to the magnetic healing length) the most energetically favorable configuration will be determined by the boundary conditions at the wall, hence $\beta = 63.4°$).

From this point we do assume that the peak (minimum) of the absorption spectrum corresponds to $\beta = 63.4°$. This is the shift we want to plot as function of temperature. The problem with this data set is that the SNR is around 3 in the normal phase, but becomes worse below the transition temperature T_c, when the absorption spectrum gets wider and the susceptibility reduces. In addition the right absorption line moves over the middle peak (signal from the channels), which increases the difficulty to determine the exact peak position.

The position of the absorption peak for the higher temperatures (around T_c) was determined with one single scan; for the lower temperatures scans needed to be averaged to get high enough SNR (for which the temperature was considered to be the averaged temperature of the scans). This averaging gradually increased to 25 line shapes for the lowest temperatures. The SNR for the right peak was better than for the left peak, and the shifts could be observed for temperatures till 0.6 T_c. For the left peak the SNR [55] becomes too low for temperatures under 0.85 T_c. This is partly due to lower SNR for the left peak, but also because of the subtraction of the baseline,

[55] One can consider averaging even more, but if one averages over a too long temperature range the absorption spectrums will hardly overlap (as they have shifted too much). In that case averaging does not even help to increase the SNR.

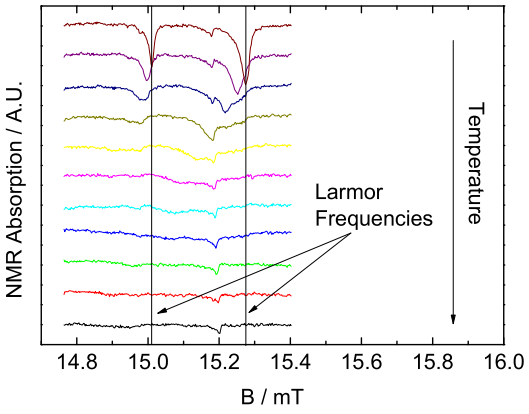

Figure 4.17: This is a 2D projection of figure 4.15. The colors of the absorption lines do represent the same temperature. The function of this illustration is to show how the absorption line shifts away from the Larmor frequency. All line segments away from the Larmor frequency do correspond with a β larger than 0 and maximally 63.4°. Not only becomes the absorption peak broader, as expected as the $\hat{\mathbf{n}}$-vector bends over the sample, but also becomes asymmetric with the minimum of this absorption line positioned at the left side. It means that the $\hat{\mathbf{n}}$-vector has in most part of the sample an angle with the magnetic field corresponding to this line segment, and as this minimum is most left of the broadened absorption line, it is reasonable that it would correspond to the maximal achievable angle, which is 63.4°. This idea is strengthened by the realization that for these narrow cylinders (small compared to the magnetic healing length) the most energetically favorable configuration will be determined by the boundary conditions at the wall, hence $\beta = 63.4°$).

which is for the raw data much more curved at the position of the left peak than for the right peak.

As already mentioned, for some peculiar reason the resonance frequencies of the absorption spectrums seem to happen at different magnetic fields. This has probably to do with the distribution of the magnetic field lines through the sample, but (at least in the normal state) we do know they should all be in resonance at the Larmor frequency, which is in our case equal to the resonance frequency of the tank circuit, hence 488867 Hz. For this reason all shifts are expressed relative to this frequency. So the frequency shifts of the absorption peaks, which we believe to correspond with $\beta = 63.4°$, as function of reduced temperature for 0.5 and 4 bar are plotted in figures 4.18 and 4.19, respectively. All curves are fitted with equation (4.38).

The fit parameters, which are obtained by least square fit methods, are not deter-

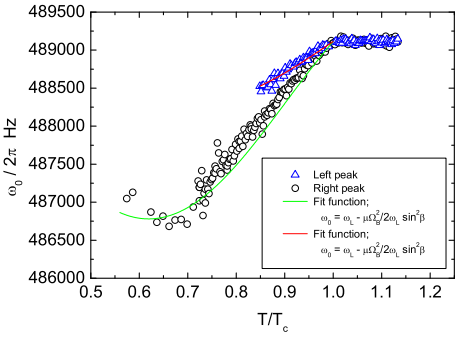

Figure 4.18: Shifts of the absorption peak at 0.5 bar, for $\beta = 63.4°$. The blue open triangles and the black open circles correspond to the shifts of the left and right peak in figure 4.15, respectively. Both shifts are fitted with equation (4.38), for which the results are discussed in the text. The shift of the blue data is less than the black data, from which it can be concluded that the solid/liquid ratio must be higher. Interesting to observe in the black data is that for low enough temperature the shift is reversed, because the magnetization of the solid is still increasing, while the susceptibility of the superfluid is decreasing.

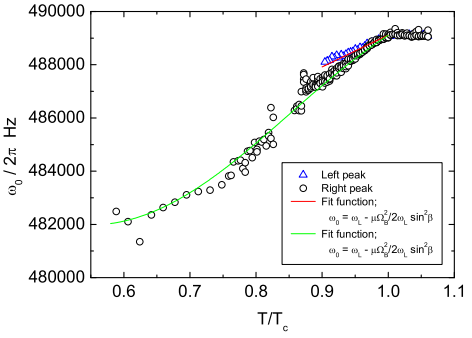

Figure 4.19: Shifts of the absorption peak at 4.0 bar, for $\beta = 63.4°$. The blue open triangles and the black open circles correspond to the shifts of the left and right peak in figure 4.15, respectively. Both shifts are fitted with equation (4.38), for which the results are discussed in the text. The shift of the blue data is less than the black data, from which it can be concluded that the solid/liquid ratio must be higher. The lack of black data points near 0.85 T_c is due to the difficulty to determine the positions of the peak as it shifts through the middle peak.

mined for each pressure individually. For each pressure we filled in the known values of equations (4.38) and (4.39), leaving only the temperature dependence and the fit parameters n_{sol}/V_{liq} and θ. We do assume that the Curie-Weiss constant θ and the amount of solid atoms (in mole) per liquid volume n_{sol}/V_{liq} are the same for all (our used) pressures and temperatures. It means that these parameters could be determined by multiple fits at different pressures. The parameters which collectively gave the best fit of the data was considered to be most reliable of describing the conditions of our cell. The data for 0.5 and 4 bar inclusive these fits are put in figure 4.18 and 4.19.

In summary, it was not easy to fit these data as the main problems were:

- The SNR for the lowest temperatures was very small.
- The signal of opens spaces are still an ensemble of many space, which have in principle all their own n_{sol}/V_{liq} ratio.
- The absorption peak was considered to belong to $\beta \approx 63.4°$, which can be in reality smaller.
- Results were obscured as the signal shift through other absorption lines.

Nevertheless, we do see that this model describe the physics quite well. In detail there may be some deviations, which are likely due to uncertainty about the exact geometry of our system.

In overall the best fit parameter for n_{sol}/V_{liq} was 68.95 and 17.85 mole m^{-3} for left and right peak, respectively. θ was found to be 0.3 mK. Of course this ratio is a bit different from the ideal case, as the open spaces will be packed worse and/or are partly filled with stycast. Nevertheless, as we assume that the left peak is indeed from the signal between the fibers and the right peak at the wall, the calculation does not differ more than a factor 1.7 compared to the ideal calculation. This is surprisingly good as the density of the solid layer is in general hard to guess, and the fibers seem to be well packed. It should be mentioned that most probably the smallest spaces had difficulties to be completely filled with stycast. As in the case of the fibers they were typically sucked in the stycast for 5 mm. If the same thing happened for the smallest spaces between the fibers, it is not a surprise that these spaces became available, when the fibers were reopened.

This model is very helpful to understand any deviation of the bulk B-phase (or A-phase) in samples with relative high solid to liquid ratios. For example the data obtained in aerogel, see [127] and [132]. These samples are highly porous (typically 98%), and as a consequence surface and volume are randomly distributed over the sample. If one deals with the B-phase in such a sample, one can imagine that the $\hat{\mathbf{n}}$-vector is also randomly distributed over the sample. The advantage of our geometries is that there is a clear orientation of the $\hat{\mathbf{n}}$-vector, for which evidently a shift is expected. These shifts are visible in our data, from which it is clear (if one compares with the bulk) that the interaction (rapid exchange) with the solid does influence the

amplitude of the total shift. One can even see, best noticeable in figure 4.18, that for low enough temperatures the total magnetization of the solid (also the decrease of the susceptibility of the B-phase) is enough to shift back the absorption peak in the direction of the Larmor frequency. What is a bit unclear to the author is how 'far' the solid influences the liquid. It is clear that there will be an exchange between the atoms at the solid/liquid interface, but unclear how the interaction reduces over space. In our geometry there is clear spatial distribution between wall and volume, this in contrast for example with aerogel, for which one can imagine that the atoms near the wall (still most atoms are in the liquid) are more influenced by this rapid exchange than the atoms in the center. An additional difficulty, to see if some atoms are more affected, is that the Cooper pairs at the wall are also the ones for which the $\hat{\mathbf{n}}$-vector has the largest angle β with respect to the magnetic field. Nevertheless, it seems that the whole liquid is coherently influenced by the solid, for which is looks like that this model is also valid for cylindrical-like samples.

4.6 Conclusion

We have shown that the channels in the PCF are good candidates for long cylindrical samples. They could be made macroscopically long, while the diameter had only little deviation. Also the roughness was small and had only an amplitude of approximately 0.5 nm, the same order of magnitude as the size of ^{3}He atom. It also seems to have a correlation length of 26.5 nm, which may be close to the size of the Cooper pairs of ^{3}He, but as this amplitude is small as well, it was never considered a problem to form a superfluid inside these channels. We conclude that this geometry would be perfect to study exotic superfluid states, like the polar phase and/axial phases at low pressures.

As the filling factor of this sample is extremely small, we were very delighted that we obtained such high SNR (~ 3), due to the ultra-high Q of our tank circuit, for our desirable temperature sweeps combined with our used bandwidth (~ 2.6 Hz). So, it turned out that the weakly coupled transformer technique was suitable to measure a μmole of ^{3}He *at low frequencies*, and as this is a completely passive system, it is suitable to continue measurement for weeks.

The failure to observe any frequency shift (relative to the Larmor frequency) made it hard to conclude with any certainty if there was a superfluid acquired inside these channels. At least it can be concluded that the superfluid B-phase was not observed for temperatures at 300 μK till 10 bar. By itself a surprising result, as the suppression was (theoretically) not expected to be that much. To exclude that any polar or axial state was formed, a modification of the system is required.

As the production of the bundle of fibers apparently left some open space between them, it was a fortunate opportunity to study the superfluid in these kinds of vol-

umes. This study was definitely made easier as for some unknown reasons locally the magnetic field in this volumes was slightly different, so the NMR signals corresponding to the volumes could be distinguished. As the cross section of these volumes allows the formation of the B-phase, it is an interesting size in the sense that the total magnetization of the solid (2 layers of ^{3}He adsorbed to the wall) comes close to that of the liquid. This in a perfect condition to study the rapid exchange between the solid and liquid, and it is found that even in a cylindrically shaped volume the liquid coherently interacts with the solid layer.